AN INVESTIGATION INTO THE DESIGN OF HOLLOW ACCUMULATOR ROLLS USING FINITE ELEMENT ANALYSIS

by

Anthony V. Viviano

Submitted in Partial Fulfillment of the Requirements

for the Degree of

Master of Science

in the

Mechanical Engineering

Program

YOUNGSTOWN STATE UNIVERSITY

June, 1998

AN INVESTIGATION INTO THE DESIGN OF HOLLOW ACCUMULATOR ROLLS USING FINITE ELEMENT ANALYSIS

by

Anthony V. Viviano

I hereby release this thesis to the public. I understand this thesis will be housed at the Circulation Desk of the University library and will be available for public access. I also authorize the University or other individuals to make copies of this thesis as needed for scholarly research.

Signature: _____ 6/8/98

Student Date

Approvals:

_____ 6/8/98

Thesis Advisor Date

_____ 6/8/98

Committee Member Date

_____ 6/8/98

Committee Member Date

_____ 6/8/98

Dean of Graduate Studies Date

ABSTRACT

Accumulator systems consist of a series of rolls arranged either vertically or horizontally which are used in many sheet processing lines for the purpose of storing up strip. Strip is stored so that when supply coils run out new coils can be welded to the ends of old coils without stopping the entire line. Literature on roll design is scarce because companies that have developed present design practices are reluctant to offer this knowledge.

Given the fact that many rolls make up some accumulator systems, the cheaper manufacturing costs associated with some designs would be very desirable providing the design is acceptable. Much of the present design theory is based on a static analysis assuming the load from the strip is evenly distributed over the roll and there is negligible loss of load in the strip going from one side of the roll to the other. A previous thesis done on this subject focused on modeling the roll using finite element analysis, FEA, and making these same assumptions. This research focuses on using FEA with nonlinear contact elements located between the strip and roll in order to allow the software to distribute the load from the strip to the roll. From the results of this analysis it will be reasoned whether the present design assumptions concerning load transferal are valid or not and a goal of this investigation is to verify or discount the previous work that was done.

ACKNOWLEDGMENTS

Dr. Daniel H. Suchora - Thesis Advisor

Dr. H. W. Kim - Thesis Committee

Dr. Robert A. McCoy - Thesis Committee

TABLE OF CONTENTS

LIST OF FIGURES

LIST OF TABLES

LIST OF SYMBOLS

E	modulus of elasticity
F	force, ratio of static to dynamic coefficients of friction
f	frictional force
$FACT$	ratio of static to dynamic coefficients of friction
f_n	normal force
f_s	tangential force
$\bar{f}_s$	limiting sliding force
g	gap
h	typical target length
I, J, K, L	target nodes
KN	normal contact stiffness
KT, K_t	tangential contact stiffness
M	contact node
MU	coefficient of friction internal to ANSYS®
N	normal force
r	radius
s, t, n	target surface natural coordinate system
(s^*, t^*)	contact node location
T_1	belt tension opposite the direction of motion
T_2	belt tension in the direction of motion
u	total motion of contact node
X, Y, Z	global rectangular coordinate system
x, y, z	rectangular coordinate system
x_e, y_e, z_e	element force rectangular coordinate system
β	angle of belt contact
ε	user-defined compatibility tolerance in ANSYS®
λ	Lagrange multiplier force
μ	coefficient of friction
ν	Poisson's ratio, tangential displacement
θ	angle

Chapter 1: BACKGROUND

1.1 INTRODUCTION

Accumulator systems are used in processing lines whenever it is necessary to accumulate the line material in order to perform another task that requires a portion of the material to stop. For the steel coil processing industry this is commonly done with several vertically or horizontally mounted rolls, called accumulator rolls. When the coil feeding the line runs out, a portion of the line is stopped while a new coil is welded to the end of the old coil. While this portion of the line is stopped the strip that was built up in the accumulator system feeds the still running portion of the line. Then, when the new coil is ready, the stopped portion of the line is started and the accumulator system begins to build up strip again. Figure 1.1 shows a typical arrangement of accumulator systems in a processing line.

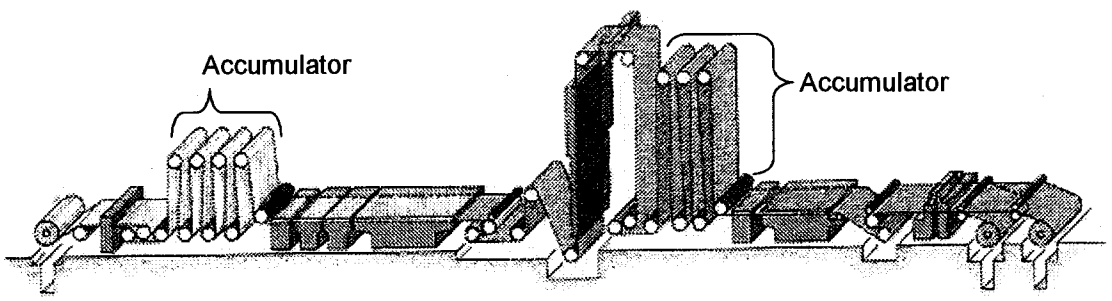

FIGURE 1.1 Typical accumulator systems in a processing line

The problem from which this investigation originated was a roll manufacturer's request to know the difference between two of their designs, both accumulator rolls, but one considerably cheaper to manufacture than the other. Given the fact that many rolls make up some accumulator systems, the cheaper manufacturing costs associated with some designs would be very desirable providing the design is acceptable.

1.2 ROLL CONSTRUCTION

Accumulator rolls vary widely in design. An actual accumulator roll design used in the past and the one analyzed in this paper is shown in Figure 1.2.

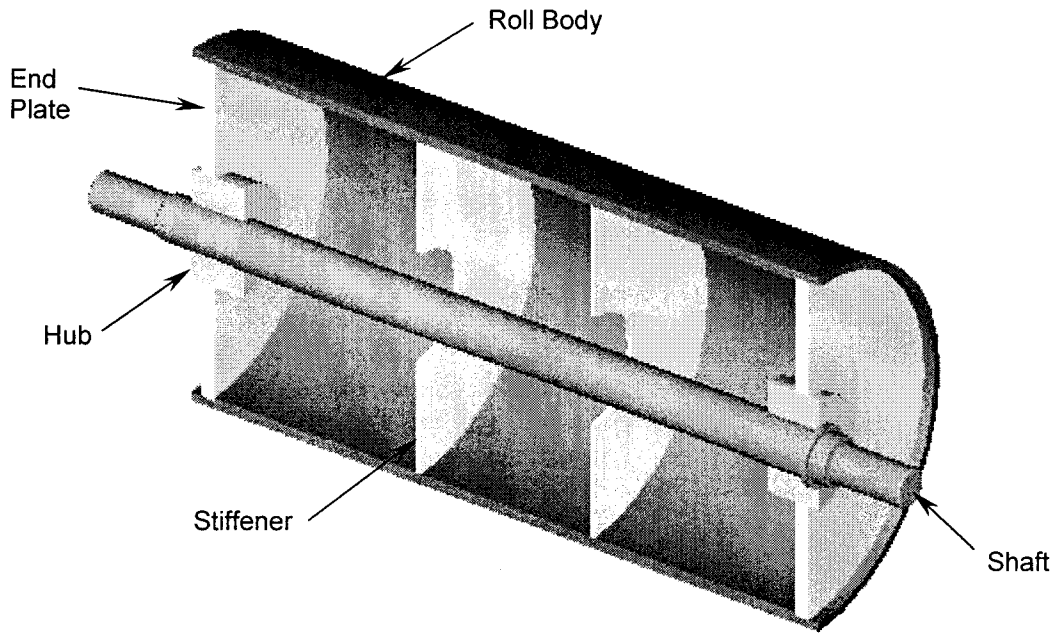

FIGURE 1.2 Accumulator roll construction

The roll is constructed from the roll body which has end plates welded onto each end. Hubs are welded to each end plate and the shaft is pressed into the hubs.

There are transverse stiffeners located at intermediate points along the roll body. These are used to help stiffen the roll body to prevent excessive deflections. Roll dimensions vary widely depending on the application; the roll analyzed in this investigation had a 60" length, 32" OD, and 1" thick roll body. The hubs had a 10" OD and 5" length. The end plates were 1¼" thick. The shaft was 4" in diameter and 77½" long. The stiffeners were ½" thick and had a 10" ID. The shaft and roll body are made from 1045 steel and the other components of the roll are made from 1018/1020 steel. Figure A.1, located in the appendix, is a drawing of this roll.

1.2 METHOD OF INVESTIGATION

Previous work was done on accumulators using the finite element analysis (FEA) software Algor®, which could not simulate the contact interface between the strip and roll. Therefore, this analysis was done using the FEA software ANSYS® which was chosen because of its extensive element formulations in the area of nonlinear contact elements. The actual contact interface between the strip and roll, including friction, was simulated and the overall resulting stresses and deflections were compared to the work done previously.

Chapter 2: PREVIOUS RESEARCH

2.1 ASSUMPTIONS

A previous thesis was done on this subject using the FEA software Algor®. It was desired to develop a static FEA model that would aid in the design of hollow steel accumulator rolls. This work was done as a first approximation and developed some of the basic assumptions necessary to perform the analysis as well as lay the foundation for future work. Several assumptions had to made because of the complexity of the problem and the limited capabilities of the FEA software. The first of these was the use of a static analysis. Although the spinning accumulator rolls are a dynamic phenomenon, they were modeled using a static FEA model. The reason a static analysis of this dynamic situation is permitted is because of the following logic.

The accumulator rolls are idler rolls and therefore are not driven rolls. This means that except at line startup and shut down, when line tensions will vary, the line reaches a steady-state condition and the tension in the strip on either side of an accumulator roll is approximately the same. Therefore, it is approximately the same as having a stationary roll with the strip wrapped around it and the same tension applied to both ends of the strip.

The second and third assumptions made were also because of the limited capabilities of the FEA software. Algor® did not have contact elements, therefore, the load transferal and load distribution from the strip to the roll could not be simulated by the FEA model. So a uniform pressure distribution in the radial and longitudinal directions was used and any friction developed between the strip and roll interface was ignored.

The last assumption made had to do with the shaft design. It was reasoned that shaft design is well-documented in ASME codes and therefore would not be a relevant consideration in this project. It was thought that more of the focus of this research be on the actual roll design; the endplate, roll body, and stiffener.

2.2 FEA MODEL

The model used consisted of three different elements. The shaft was modeled with beam elements. The hub and end plate were modeled with brick elements, while the roll body and stiffener were modeled with plate elements. The connection between the shaft and hub was modeled with "very stiff" beam elements, eliminating the need to model the shaft with brick elements. The model used is shown in Figure 2.1. Several models were made that varied the endplate thickness, roll body thickness, stiffener thickness, and stiffener location along the length of the roll. Tables A.1, A.2, A.3, and A.4 in the appendix of this paper summarize the model configurations that were analyzed.

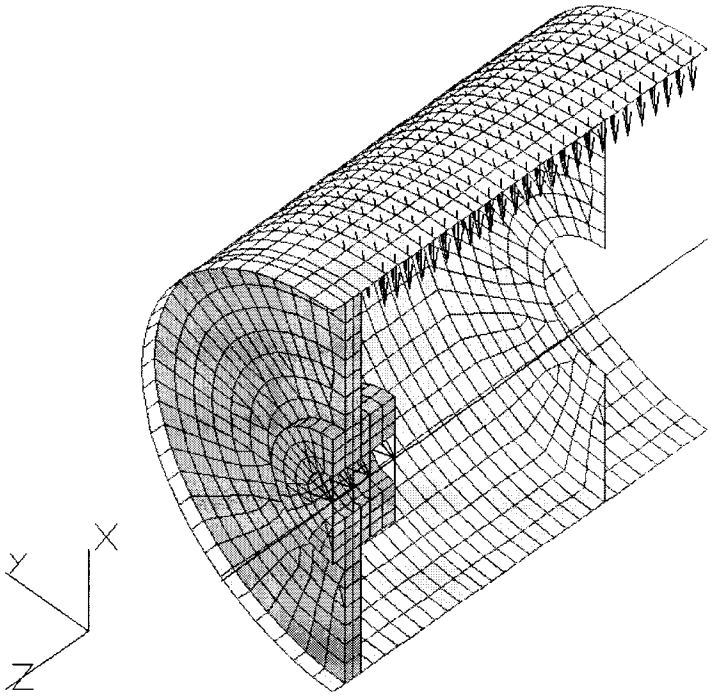

FIGURE 2.1 Algor® FEA model of roll showing uniform pressure loading

2.3 RESULTS

Portions of the Algor® analysis results are contained in Chapter 6 where they are compared to the ANSYS® analysis results. Numerous roll configurations were considered for the purpose of establishing a trend that would show what variations in the roll configuration that would lead to a more efficient and better roll design.

Chapter 3: FEA VERIFICATION

3.1 THEORY

When using FEA to analyze complicated problems, it is good practice to try to verify the solutions obtained. There are different methods of verification commonly used. If a by-hand or theoretical solution exists, this provides a good comparison for the FEA. If experimental work was performed and actual result data exists, then this also is a good means of verifying the FEA. If neither of the above methods can be obtained and the problem is complex, an FEA can be performed on a similar problem with a known solution. Then, the FEA of the similar problem can be verified and deductions can be made from it to help verify the FEA of the actual problem. Since no theoretical solution exists for this problem and no experimental work has been performed, a similar problem with an existing solution was sought.

3.2 FRICTIONAL FORCES ON FLAT BELTS

Due to the nature of this problem, particularly how the strip is wrapped around the roll, a comparison can be made to that of a flat belt wrapped around the curved surface of a pulley. The frictional forces that develop between the belt and the pulley's surface have been studied in the past. A flat belt and pulley model was developed and its theoretical solution was based on the formulation

for frictional forces on flat belts found in Hibbeler [2]. Figure 3.1 shows a flat belt wrapped around the curved surface of a pulley by an angle of contact β.

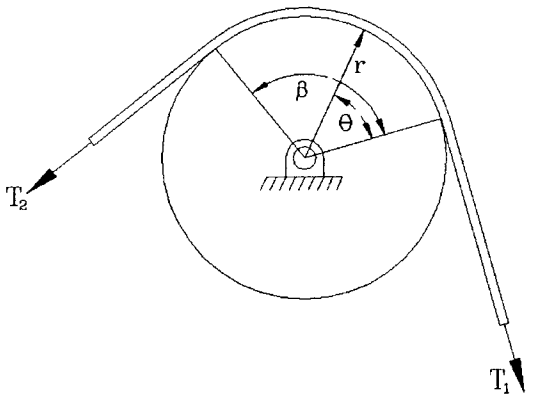

FIGURE 3.1 Flat belt wrapped around pulley by contact angle β

The coefficient of friction at the interface of the two surfaces is μ. The tension in the belt varies from T_1 to T_2 such that $T_1 < T_2$. To determine the tension T_2 consider Figure 3.2.

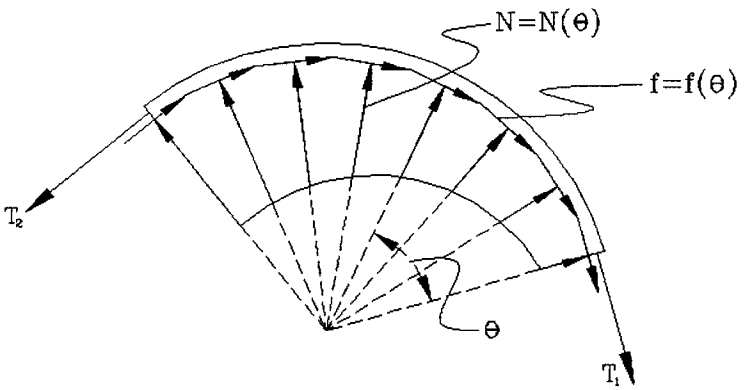

FIGURE 3.2 Free body diagram of contacted belt segment

The normal force, N, and frictional force, f, both vary as a function of θ. Isolating a differential element of the belt, as shown in Figure 3.3, and assuming

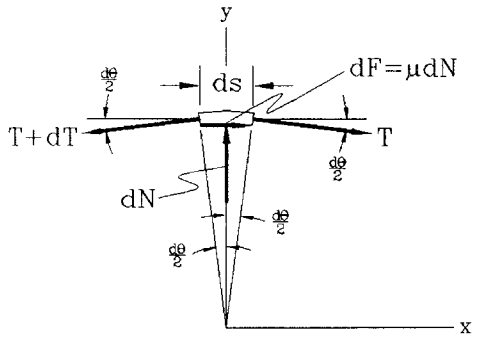

FIGURE 3.3 Free body diagram of a differential element of the belt

either impending motion or motion of the belt, the magnitude of the frictional force can be written as:

$$df = \mu\, dN$$

This frictional force opposes the sliding motion of the belt, which increases the magnitude of the tension in the belt by an amount dT. Applying the equilibrium equations to the free body diagram of the differential element of the belt:

$$\overset{+}{\rightarrow}\sum F_x = 0 \;\Rightarrow\; T\cos\left(\frac{d\theta}{2}\right) + \mu dN - (T+dT)\cos\left(\frac{d\theta}{2}\right) = 0 \qquad (3.1)$$

$$\overset{+}{\uparrow}\sum F_y = 0 \;\Rightarrow\; dN - (T+dT)\sin\left(\frac{d\theta}{2}\right) - T\sin\left(\frac{d\theta}{2}\right) = 0 \qquad (3.2)$$

Since $d\theta$ is infinitesimal in size, the following terms in equations 3.1 and 3.2 can reduce to:

$$\sin\left(\frac{d\theta}{2}\right) = \frac{d\theta}{2} \quad \textit{and} \quad \cos\left(\frac{d\theta}{2}\right) = 1$$

and the product of the two infinitesimals dT and $d\theta/2$ may be neglected when compared to the infinitesimals of the first order. So rewriting 3.1 and 3.2 as 3.3 and 3.4 respectively:

$$\mu dN - dT = 0 \qquad (3.3)$$

$$dN - Td\theta = 0 \qquad (3.4)$$

Eliminating dN from 3.3 and 3.4 the following relation can be written:

$$\frac{dT}{T} = \mu d\theta \tag{3.5}$$

Now, integrating equation 3.5 between the points of contact that the belt makes with the pulley and defining $T = T_1$ at $\theta = 0$ and $T = T_2$ at $\theta = \beta$ yields the following:

$$\int_{T_1}^{T_2} \frac{dT}{T} = \mu \int_0^{\beta} d\theta \tag{3.6}$$

$$\ln \frac{T_2}{T_1} = \mu\beta \tag{3.7}$$

If equation 3.7 is rewritten solving for T_2 then:

$$T_2 = T_1 e^{\mu\beta} \tag{3.8}$$

$T_1 = belt\ tension\ opposite\ the\ direction\ of\ motion$

$T_2 = belt\ tension\ in\ the\ direction\ of\ motion$

where: $\mu = coefficient\ of\ friction$

$\beta = angle\ of\ belt\ contact$

$e = 2.718...;\ base\ of\ the\ natural\ logarithm$

So given a flat belt and pulley, the tension in the belt opposing the direction of motion can be found by solving equation 3.8 for T_1 if the input tension, T_2, is known:

$$T_1 = \frac{T_2}{e^{\mu\beta}} \tag{3.9}$$

The implication of equation 3.9 is that given some input tension to the belt or, T_2, a reaction tension T_1 can be found; which should equal the input tension minus any of the frictional forces developed at the belt and pulley interface.

3.3 THEORETICAL MODEL

Using the above formulation, a model of a flat belt and pulley was developed. For the model of Figure 3.1, the input tension is $T_2 = 1000lb$, the coefficient of friction is $\mu = 0.2$, and the angle of contact between the belt and pulley is $\beta = \pi / 2$. Substituting these quantities into equation 3.9 yields:

$$T_1 = \frac{T_2}{e^{\mu\beta}} = \frac{1000\,lb}{e^{0.2(\pi/2)}} = 730\,lb$$

In other words, if a tension of $1000lb$ is applied to one end of the belt then the force felt on the other end of the belt would be $730lb$.

3.4 FEA MODEL

The belt and pulley model of Figure 3.1 was modeled in ANSYS® using a ½ symmetry model. Based on the theoretical solution, the force distribution is only dependent on T_2, μ, and β, and is independent of the radius of the pulley. However, a pulley radius and width, as well as a belt thickness and width, was needed in order to perform an FEA. Referring to Figure 3.1, a radius of 2" and a width of 1" were used for the pulley and a thickness of 0.125" and a width of 1" was used for the belt. Note that because this model lends itself to ½ symmetry only 0.5" widths were used in the FEA model. The pulley was modeled using the ANSYS® SOLID45 elements. These are 3-D structural solid elements defined by eight nodes having 3-DOF associated with each node: nodal translations in the x, y, and z directions. The belt was modeled using the ANSYS® SHELL63 elements. These are 3-D elastic shell elements defined by four nodes having

6-DOF associated with each node: nodal translations in the x, y, and z directions as well as nodal rotations about the x, y, and z axes. The contact interface between the belt and pulley was modeled using the ANSYS® CONTAC49 elements. These are 3-D point-to-surface flexible-to-flexible contact elements defined by five nodes having 3-DOF associated with each node: nodal translations in the x, y, and z directions. The FEA model used is shown in Figure 3.4.

FIGURE 3.4 FEA model of belt and pulley with loads and boundary conditions

The load on the belt corresponds to the input tension of Figure 3.3. Since a half model was used, then only half the load or $500lb$ was applied to the belt. Boundary conditions holding translations in the global x-direction were applied to the other end of the belt. Boundary conditions holding translations in the global

x and y directions were applied to the center of the pulley and, of course, symmetry boundary conditions holding translations in the global z-direction were applied at the plane of symmetry of the model. Both the belt and pulley were chosen to be made of steel with a modulus of elasticity of $E = 30 \cdot 10^6 \, psi$ and a Poisson's ratio of $\nu = 0.3$. A coefficient of friction of $\mu = 0.2$ was used just as in the theoretical model. The model was developed in this manner to better match the actual strip and roll problem.

The most pertinent results of the analysis are the reactions at the opposite end of the belt from which it was loaded. The reaction solution for the selected nodes is in tabular form and is shown in Figure 3.5 along with the model.

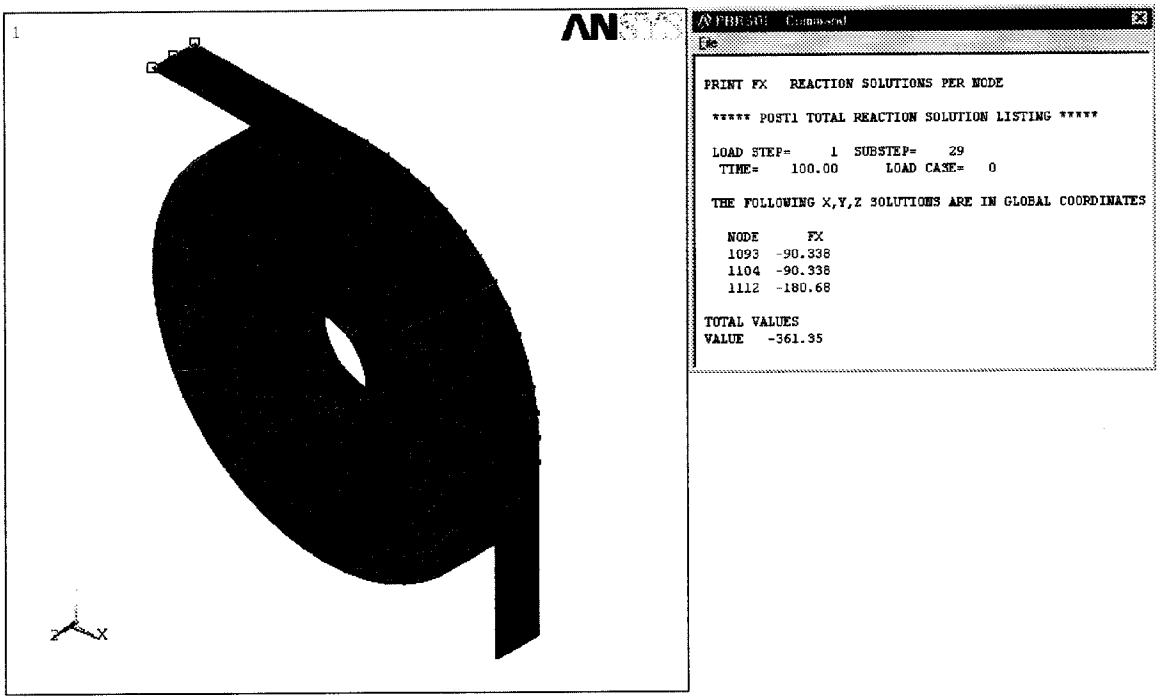

FIGURE 3.5 Reaction solution for selected nodes

Notice the selected nodes in Figure 3.5 correspond to the nodes which were fixed from translations in the x-direction. The reactions for the three selected nodes total $-361.35lb$. The negative sign indicates the reaction forces are acting in the negative x-direction as expected. These results must be doubled before they can be compared to the theoretical value, because only a ½ model was analyzed. Therefore, the total reaction force predicted by the FEA is $723lb$ which can be compared to the theoretical value for T_1 found in section 3.3 which was $730lb$. So there is approximately a 1% difference between the two values, which gives reliability to the modeling techniques and elements used in the FEA. This lays the foundation for more confident modeling of the original strip and roll problem.

Chapter 4: CONTACT ELEMENT FORMULATION

4.1 ELEMENT DEFINITION

Behind any FEA solution is the mathematical formulation of the elements used in the model. The key to the solution of this problem is the use of nonlinear contact elements. The following element definition is based on the description found in the *ANSYS® Elements Reference* [5]. The contact elements used were ANSYS® CONTAC49 3-D point to surface contact elements. This element was designed to simulate general 3-D flexible to flexible surface contact and sliding between two bodies including the effects of friction. Figure 4.1 is a schematic representation of the CONTAC49 element shown with the 2-D version CONTAC48.

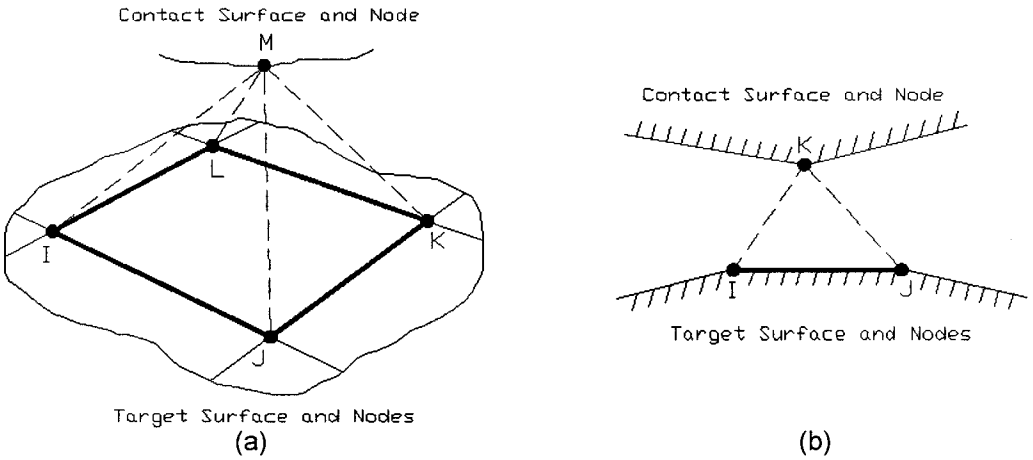

FIGURE 4.1 ANSYS® point to surface contact element (a) 3-D version CONTAC49 (b) 2-D version CONTAC48

The CONTAC49 element is a five node element consisting of a contact surface and a target surface in a pyramidal shape. There are three degrees-of-freedom

associated with each node: translations in the x, y, and z directions. The target surface has four target nodes I, J, K, and L and is the shape of a quadrilateral. The contact surface is made up of the contact node M and completes the pyramid. The target surface is made up of all the target nodes and the contact surface is made up of all the contact nodes. The first surface tangent vector is a unit vector tangent to the target surface pointing from I to J. The surface normal vector is the unit vector perpendicular to the target surface pointing out from the target surface to node M. The second surface tangent vector is the cross product of the surface normal vector and the first surface tangent vector. All vectors are defined according to a right-handed coordinate system.

A normal contact stiffness, KN, must be defined and is used to determine contact forces in the penalty function method. This penalty stiffness acts in the direction of the surface normal and is used to enforce displacement compatibility by limiting the penetration of the target surface by the contact node. The value of KN varies because it depends on both the stiffness of the material the model is made of and the geometrical stiffness of the model. KN should be large enough to prevent overpenetration but not too large that it causes convergence problems. It is recommended from the *ANSYS Analysis Guides* [4] that the following relation be used to estimate KN:

$$KN \approx fEh$$

$$\text{where}: \begin{cases} f = \text{compatibility factor varying from 0.01 to 100;} \\ \quad \text{a good initial value to use is } f = 1 \\ E = \text{modulus of elasticity of the material in contact;} \\ \quad \text{for different materials use the smaller value} \\ h = \text{typical contact target length or element size;} \\ \quad \text{square root of the target area} \end{cases}$$

A sticking contact stiffness, KT, is used to account for friction between the surfaces and it acts in the direction tangent to the target surface. KT should be 1, 2, or 3 orders of magnitude less than KN. If KT is not specified it defaults to $KN/100$. For a friction model, there is a static-to-dynamic coefficient of friction or $FACT$ that must be specified, as well as the coefficient of friction MU. ANSYS® takes the dynamic coefficient of friction as MU while it uses $FACT \cdot MU$ as the static coefficient of friction.

4.2 ELEMENT ALGORITHMS

The software uses many algorithms as described in the *ANSYS Theory Reference* [6] to determine when contact occurs between the contact and target surfaces. What ANSYS® refers to as the "pinball algorithm" determines contact to occur whenever the contact node, M, penetrates the target surface made up of nodes I, J, K, and L. For clarity consider the 2-D case shown in Figure 4.2.

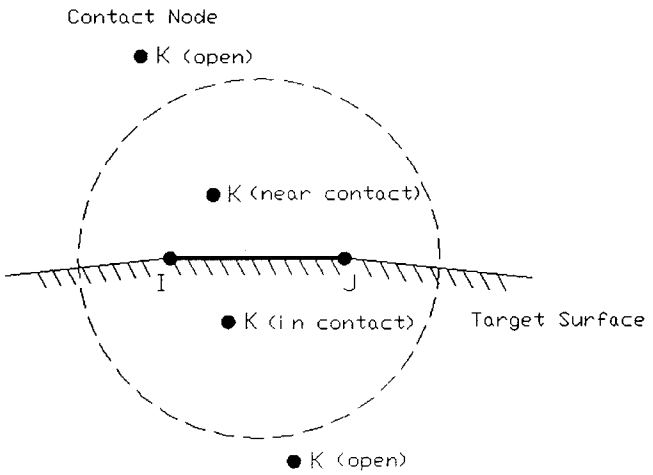

FIGURE 4.2 2-D case showing several positions of the contact node K with respect to the target surface.

Contact is determined when the contact node K penetrates the target surface made up of nodes I and J. If the contact node is outside the pinball then an open contact condition exists which means no contact is made. Contact can only occur once the contact node is within the contact circle shown in Figure 4.2. Contact occurs only when the contact node is within the contact circle and penetrates the target surface. For the 3-D case, the circle in Figure 4.2 becomes a sphere called a "pinball" whose radius is 50% greater than the larger of the two target surface diagonals.

The pseudo element algorithm associates a single target with a contact node depending on the location of the contact node in space. Pseudo elements are created every equilibrium iteration for each target surface as shown in Figure 4.3. When a contact node is found within a target's pseudo element then that contact node is associated with that target surface. It is possible that contact voids or overlaps can develop on curved surfaces due to the piecewise discretization of the curved surfaces.

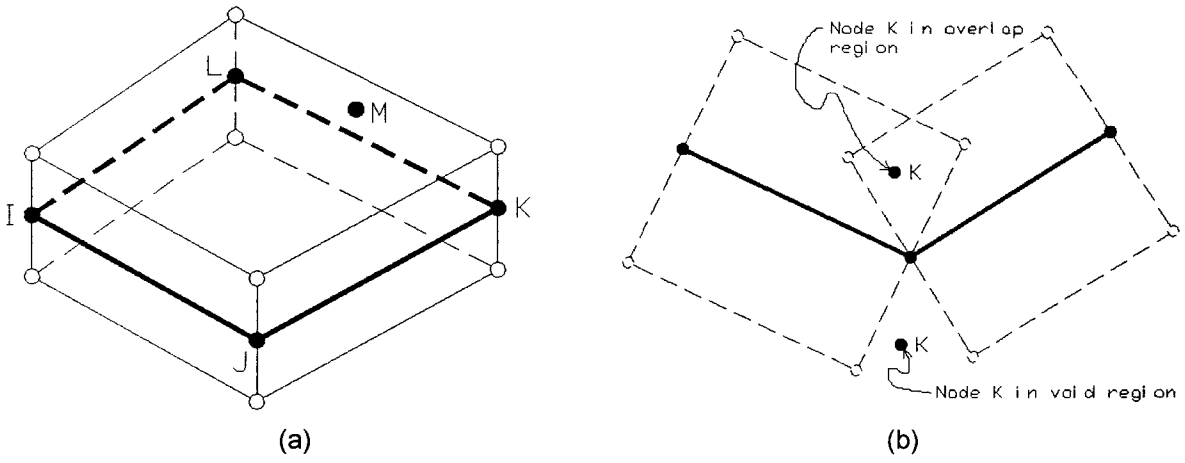

FIGURE 4.3 (a) Pseudo element created for target surface made up of nodes $I,J,K,$ and L
(b) Contact voids or overlaps occurring on curved surfaces

The two algorithms above describe the mapping between the contact node and target surface. Once the mapping is determined, then the contact node penetration on the target surface is found. The first step in doing this is to modify the target surface nodes to lie in a plane, if they do not already. Therefore, no warping of the target surface is considered. Then several coordinate systems are defined as shown in Figure 4.4.

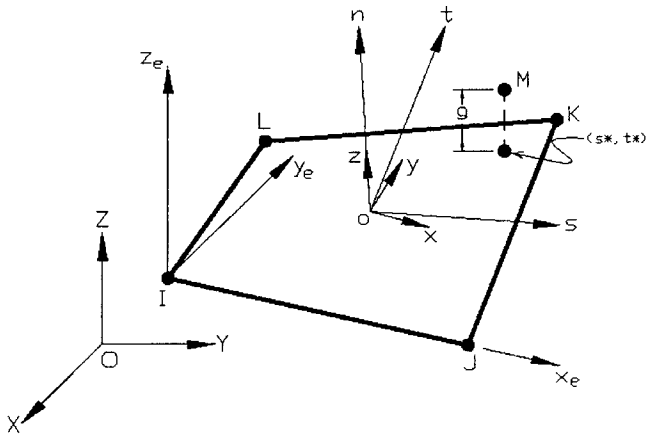

FIGURE 4.4 Coordinate systems defined to determine contact node penetration on the target surface

There is a global X, Y, Z system. Then, there is the natural s, t, n system of the planar target surface. Next, there is a rectangular x, y, z system constructed from the s, t, n system so that n and z are parallel. The last system is a rectangular x_e, y_e, z_e system used for element force output. Together these systems define the unwarped target surface.

The contact location (s^*, t^*) is determined using an iterative Newton's method based upon a normal projection of the contact node to the target plane. A value of gap or g is determined based on the contact node's location relative to

the contact surface. Contact occurs when g is found to be negative and the contact point projections s^* and t^* are found within the natural space bounds of the target. No contact occurs if a positive value of g is found.

The above algorithms are used to indicate contact between the contact node and the target surface. When contact does occur, the contact node M penetrates the target surface made up of I, J, K, and L by a magnitude of gap g. This gap violates compatibility, and forces are developed in the normal or n-direction to the target in order to reduce penetration. For friction models, frictional forces are also developed in a direction tangent to the target plane.

4.3 ELEMENT FORCES

ANSYS® uses two methods to satisfy contact compatibility. One is a penalty method and the other is a combined penalty plus Lagrange multiplier method. The penalty method satisfies compatibility by means of a user defined contact stiffness, KN, or penalty parameter. The normal force is calculated from:

$$f_n = \begin{cases} KNg & if\ g \le 0 \\ 0 & if\ g > 0 \end{cases}$$

$$\begin{aligned} & f_n = normal\ \ force \\ where: \quad & KN = normal\ \ contact\ \ stiffness \\ & g = gap \end{aligned}$$

The combined method satisfies compatibility to a user-defined tolerance by the generation of additional Lagrange or contact forces. The Lagrange multiplier component of the normal force is computed iteratively according to the following:

$$f_n = \min(0,\ KNg + \lambda_{i+1})$$

$$\lambda_{i+1} = \begin{cases} \lambda_i + aKNg & if\ |g| \geq \varepsilon \\ \lambda_i & if\ |g| < \varepsilon \end{cases}$$

Lagrange multiplier force at iteration $i+1$

$$where:\ \varepsilon = user-defined\ compatibility\ tolerance$$

$$a = iternally\ computed\ factor\ (a < 1)$$

Tangential forces arise from the friction between the contact node and target surface. The Coulomb friction model uses a user-defined coefficient of sliding friction MU. For elastic Coulomb friction, the tangential deformations of the contact node relative to the target are calculated. The total motion of the contact node M along the target plane is shown by u in Figure 4.5.

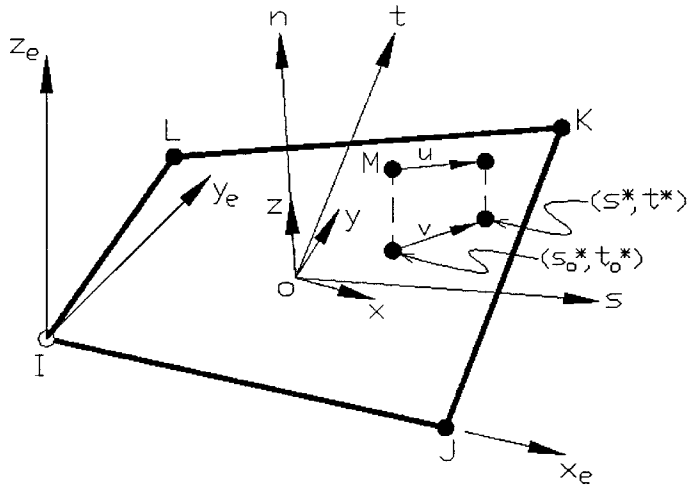

FIGURE 4.5 Motion of contact node on target plane

The total tangential displacement, v, is shown by the projection of the total contact node's motion onto the unwarped target plane. Two projected points are mapped in the natural s and t coordinate system. The current projected position of the contact node is (s^*, t^*), and the tangential deformation is tracked from the

point (s_o^*, t_o^*) which is the time point of the previously converged solution. The components of the deformation in local x-y-z-coordinate system are separated as follows:

$$v = \left(v_x^2 + v_y^2\right)^{1/2}$$

$$\text{where : } \begin{array}{l} v_x = \text{component of } v \text{ in the local } x\text{ - direction} \\ v_y = \text{component of } v \text{ in the local } y\text{ - direction} \end{array}$$

Then the deformation is further decomposed into elastic and sliding components as follows:

$$v_x = v_x^e + v_x^s$$
$$v_y = v_y^e + v_y^s$$

From these components the tangential forces are found:

$$f_x = K_t v_x^e$$
$$f_y = K_t v_y^e$$
$$\text{where : } \quad K_t = \text{sticking stiffness}$$

The magnitude of the tangential force is:

$$f_s = \left(f_x^2 + f_y^2\right)^{1/2}$$

The tangential force is divided between the sticking and sliding conditions as follows:

$$f_s = \bar{f}_s \qquad \text{if sliding}$$
$$f_s < F\bar{f}_s \qquad \text{if sticking}$$
$$\text{where : } \quad F = \text{ratio of static to dynamic coefficients of friction}$$

The limiting sliding force is:

$$\bar{f}_s = -\mu f_n$$

The previous summary is of forces which are actually computed using an approach that is similar to that of non-associative plasticity. It involves the calculation of an elastic predictor in contact traction space and is modified by means of a radial return mapping function developed by Giannakopoulos [1].

For rigid Coulomb friction, the elastic contact deformations are not considered. When the contact node penetrates the target surface the contact node is assumed to be sliding and not sticking. The tangential forces are then taken to be:

$$f_x = \frac{v_x}{v} \bar{f}_s$$

$$f_y = \frac{v_y}{v} \bar{f}_s$$

Chapter 5: FEA MODELS

5.1 ASSUMPTIONS

The assumptions made in developing the models of this investigation were taken from those of the previous research discussed in chapter two. The models developed here are still using a static analysis and therefore rest on the same logic of chapter two, which justifies a static analysis of these rolls. This is based on the fact that accumulator rolls are idler and not driven rolls and the assumption that, except during line startup and shutdown, line tensions reach a steady state condition and then tension in the strip on either side of the roll is the same.

The logic developed in the first study of assuming a uniform load distribution on the roll and ignoring the friction present at the contact interface was not used in this study. The software ANSYS® with its nonlinear contact elements was used to simulate both the load transferal and frictional effects present at the strip roll interface. Also, this analysis did not consider the roll shaft as part of the investigation because ASME standardizes shaft design.

5.2 MODELING TECHNIQUES

As shown in Figure 1.1 these rolls are mounted horizontally and the strip wraps around the roll. As seen in Figure 5.1, because of the geometry of the roll and

strip, and because of the assumption that the tension in the strip is the same on both sides of the roll, there are two planes of symmetry.

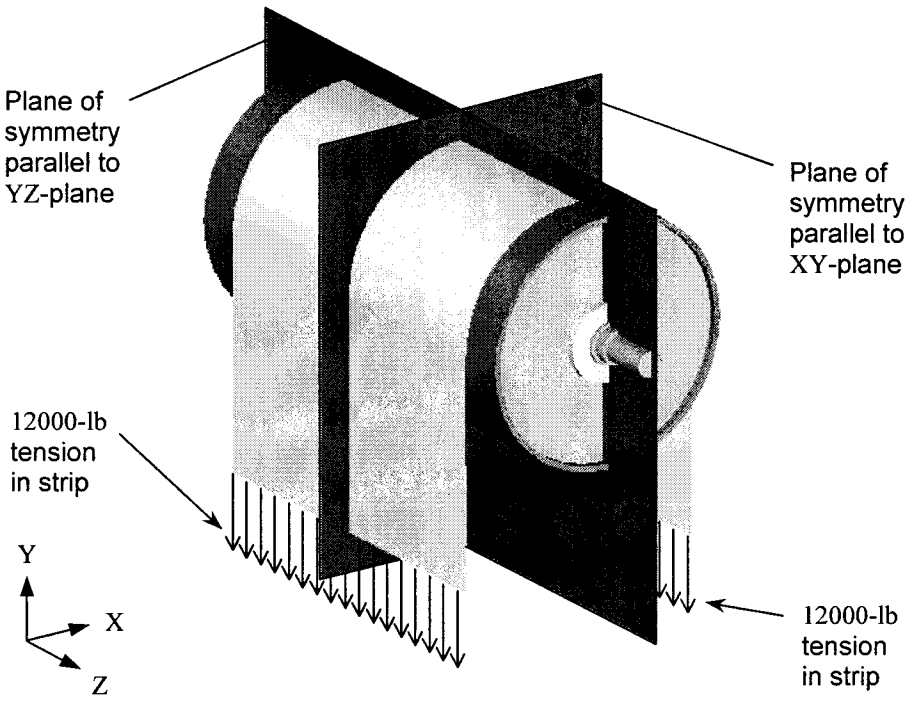

FIGURE 5.1 Symmetry that exists in roll

Therefore, it was only necessary to model ¼ of the original geometry. Note that since only a ¼ of the original geometry was used then only ¼ of the original load was applied to the model.

The strip, roll body, end plates, and stiffeners were all modeled with shell elements. This made varying the thickness of these components easier than making a new model for each case. The shaft was modeled using beam elements instead of bricks because the shaft design was not a focus of this investigation. The hub, because of its geometry, was modeled using brick elements. The connection between the shaft and hub had to be made using short "very stiff" beam elements to simulate the stiffness of the shaft where it joins the hub.

5.3 STRIP & ROLL MODELS

The strip, roll body, end plate, and stiffeners were all modeled with the ANSYS® SHELL63 element. This is a 3-D four node elastic shell element with both bending and membrane capabilities and 6-DOF associated with each node; translations in the nodal x, y, and z directions and rotations about the nodal x, y, and z axes. The hub was modeled with the ANSYS® SOLID45 element. This is a 3-D eight node structural solid brick element with 3-DOF associated with each node; translations in the nodal x, y, and z directions. The shaft and "very stiff" members connecting the shaft to the hub were modeled with the ANSYS® BEAM4 element. This is a 3-D elastic beam element with tension, compression, torsion, and bending capabilities and 6-DOF associated with each node; translations in the nodal x, y, and z directions and rotations about the nodal x, y, and z axes.

There were three base models that were developed; the first modeled a roll with two stiffeners, the second modeled a roll with one stiffener, and the third modeled a roll with no stiffeners. The ¼ model of the two-stiffener roll is shown, for clarity, in two different isometric views in Figure 5.2. Variations of the roll body and end plate thickness were also analyzed in this model. The second FEA model shown in Figure 5.3 was developed to model a roll with a single stiffener located at the midpoint of the roll body. This model was also analyzed with variations of the roll body and end plate thickness.

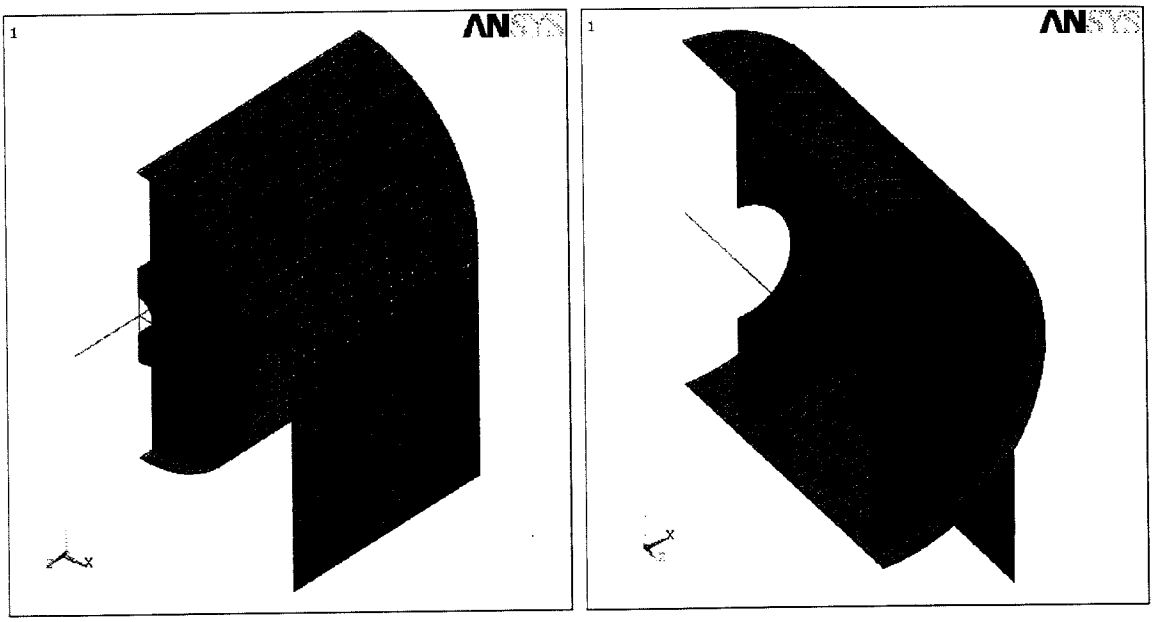

FIGURE 5.2 FEA ¼ model of the two-stiffener roll

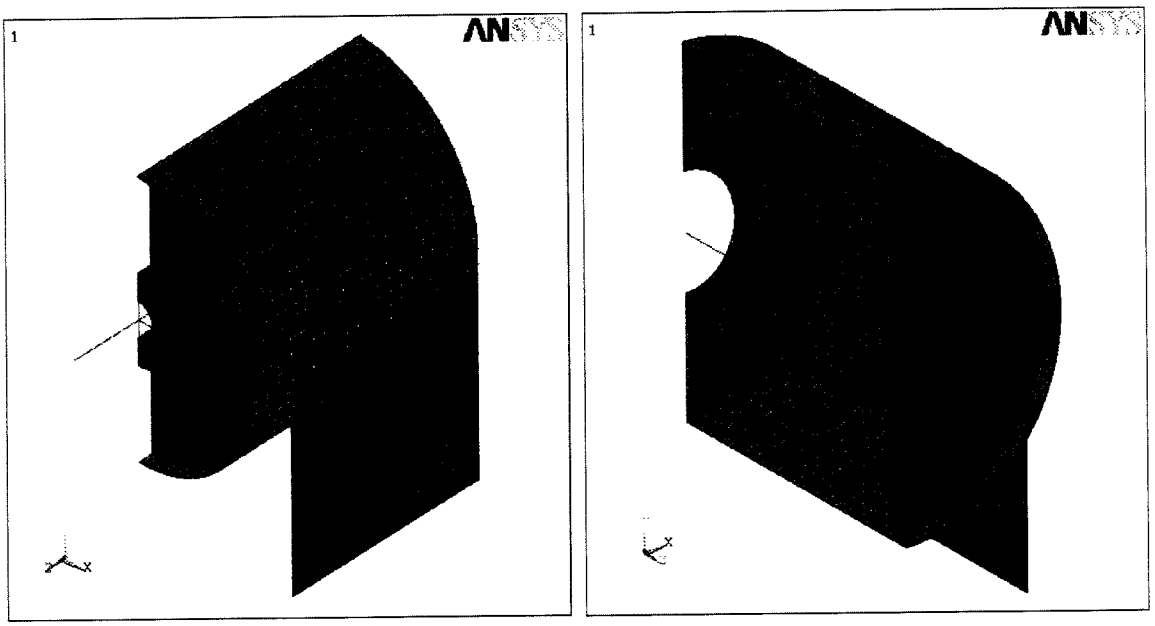

FIGURE 5.3 FEA ¼ model of the roll with a single stiffener at roll body midpoint

The last model developed is shown in Figure 5.4 and was similar to the other two models except it had no stiffeners at all, depicting an accumulator roll with no stiffeners.

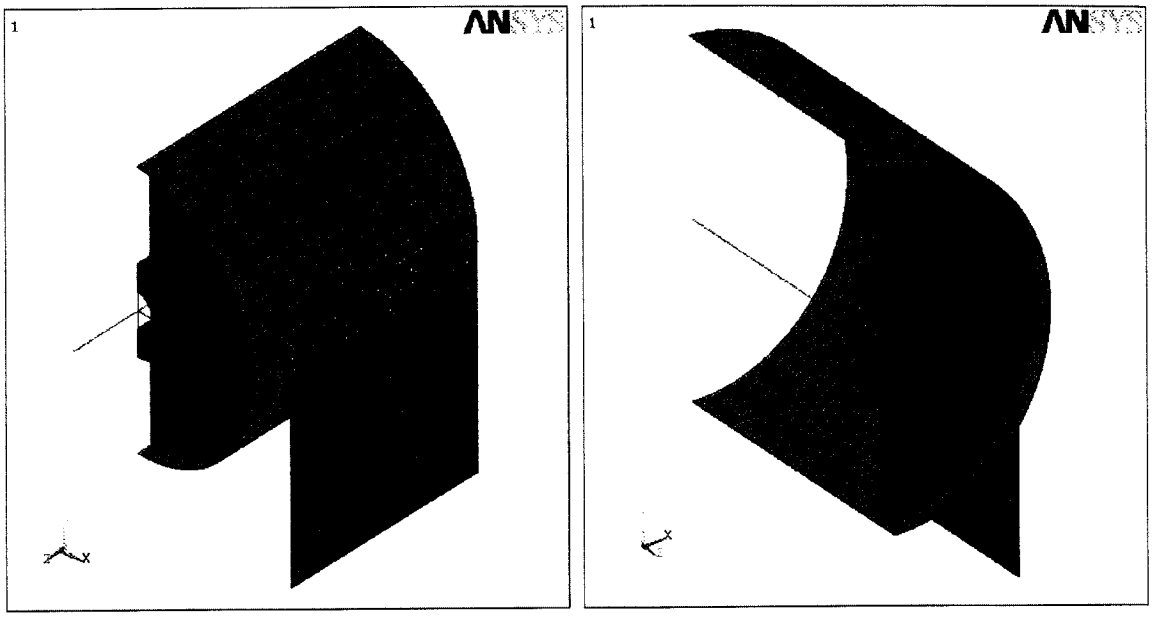

FIGURE 5.4 FEA ¼ model of the roll with no stiffeners

As with the other two models this model was analyzed with variations of the roll body and end plate thickness. All the models run were loaded and constrained in the same manner. Figure 5.5 shows the first model loaded and constrained with boundary conditions.

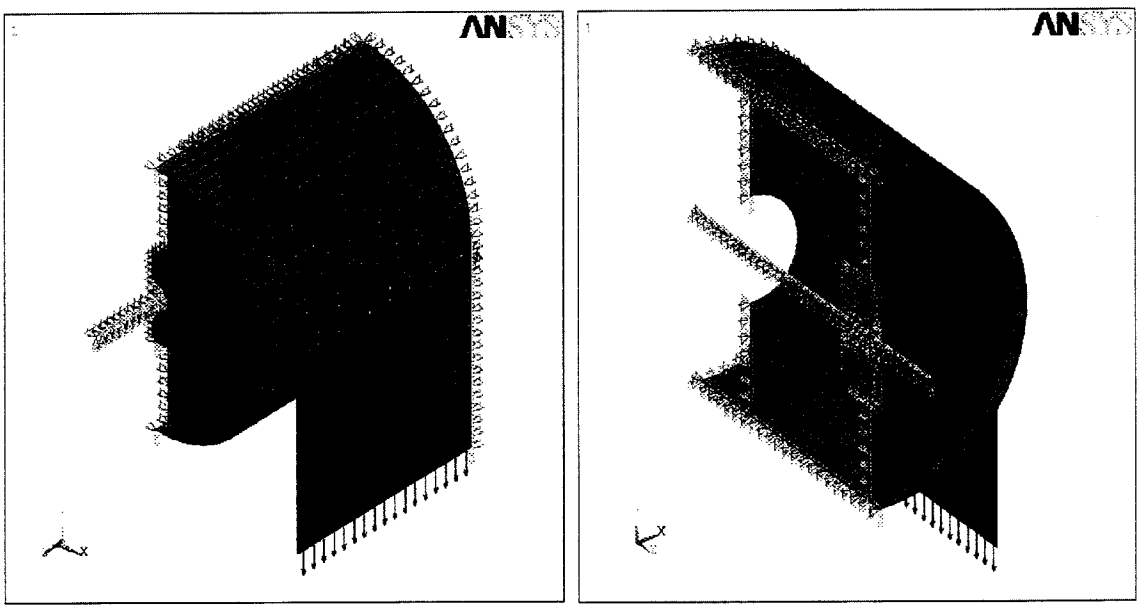

FIGURE 5.5 Loads and boundary conditions on models

The load on the ¼ model was a 6000-lb distributed load applied to the elements on the edge of the strip. Symmetry boundary conditions were applied to the nodes in the planes of symmetry and boundary conditions holding translations in the Y-direction were applied to the end of the shaft simulating how the bearing would restrain the shaft.

The different variations of the base models that were analyzed are summarized in Table 5.1. Each model that was run in this analysis was a model configuration in the previous work, therefore the results could be compared directly.

Table 5.1 Roll Configurations of Models Analyzed in ANSYS®

Case	Number of Stiffeners	Stiffener Location (in)	Stiffener Thickness (in)	Roll Body Thickness (in)	End Plate Thickness (in)
1a	2	8.25	0.5	1	1.25
1b	2	8.25	0.5	1	1
1c	2	8.25	0.5	0.75	1.25
2a	1	0	0.5	1	1.25
2b	1	0	0.5	1	1
2c	1	0	0.5	0.75	1.25
3a	0	none	none	1	1.25
3b	0	none	none	1	1
3c	0	none	none	0.75	1.25

From the results of the previous work it was noticed that varying the stiffener thickness and its location other than the three configurations above did not make substantial differences in stresses and deflections and therefore were not varied in this analysis. Based on the many roll configurations considered in the previous work it was determined only a few of the original configurations considered were necessary to make a comparison and judgements about accumulator roll design.

5.3 RESULTS

The results of this research consist of the force distribution on the roll body from the strip and, stresses and deflections in each component of the accumulator roll. For each model analyzed the force distribution on the roll body, in the normal and tangential direction, was studied. For all the cases considered there was virtually no difference in force distribution from the strip to the roll. This is attributed to the fact that the roll body thickness was only varied from 0.75" to 1", which means that the roll body was thick enough to adequately disperse the load throughout the roll body and did not permit load concentrations to develop at locations such as the stiffener. The reason roll body thickness under 0.75" were not considered was because it was thought relative deflections of the roll body would prove to be too large and may cause the strip to wrinkle. The typical normal force distribution on the roll body is shown in Figure 5.6.

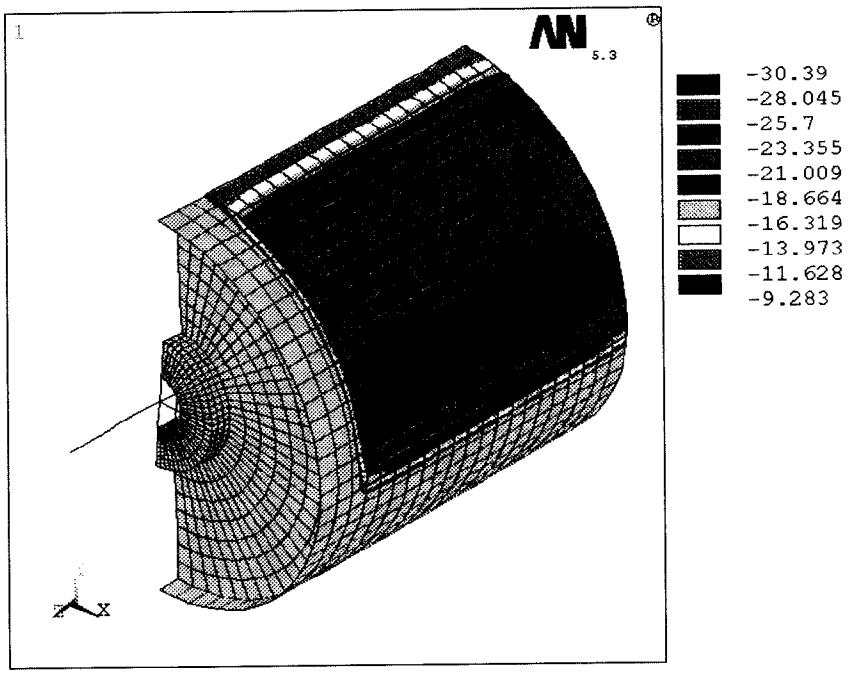

FIGURE 5.6 Normal force distribution on roll body (lb)

Careful study of Figure 5.6 shows the normal force varies somewhat in the radial direction from 9.283 lb to 30.39 lb but does not change much in the longitudinal direction. Figure 5.7 shows a planer cylindrical plot of the normal force as a function of contact angle, located at an intermediate location along the roll body. This plot is shown along with the roll body for clarity.

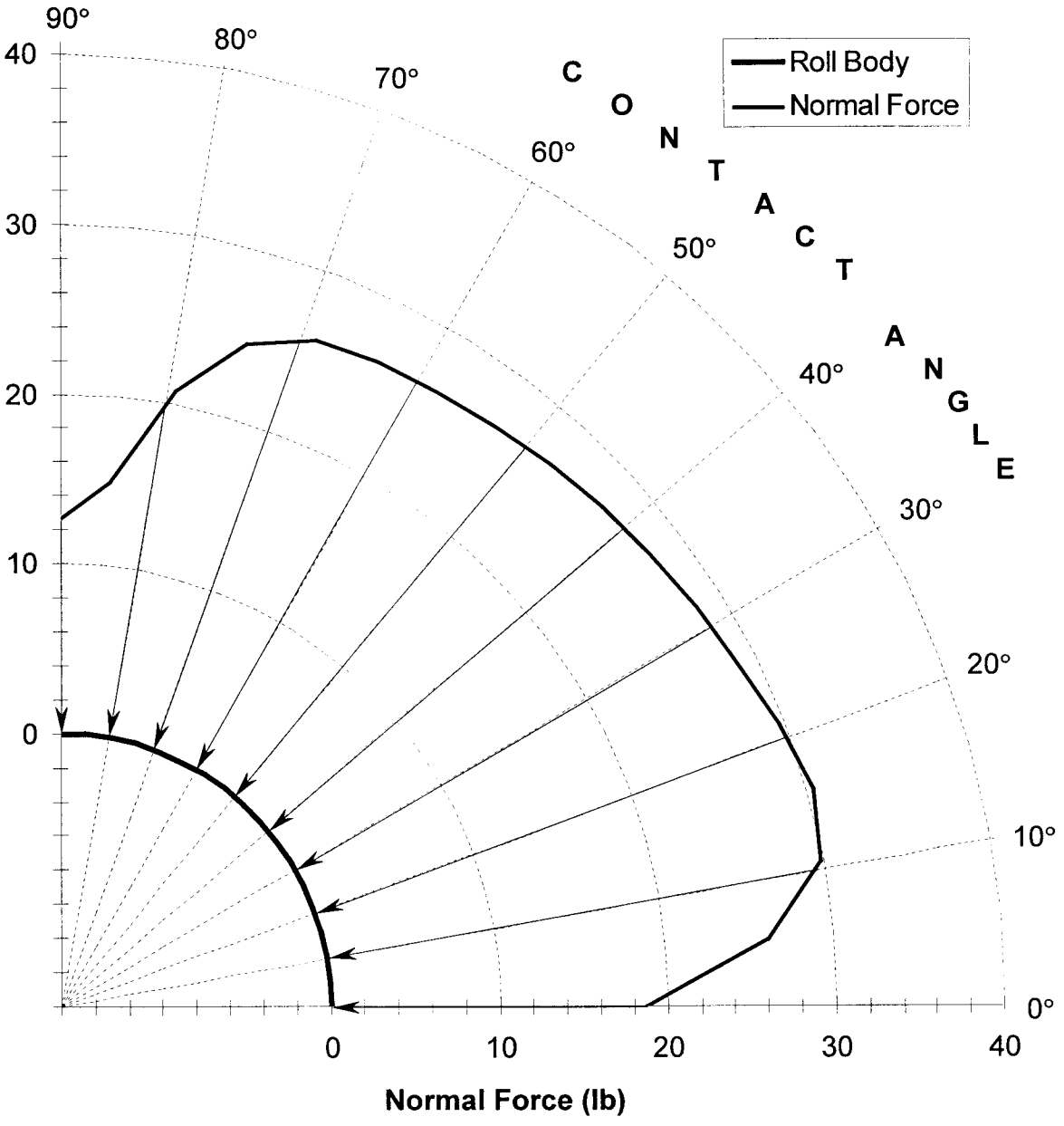

Figure 5.7 Normal force distribution as a function of contact angle

As can be seen, the maximum normal force on the roll is 30.39 lb and occurs at approximately 15° above the horizontal. The typical tangential force distribution on the roll body is shown in Figure 5.8.

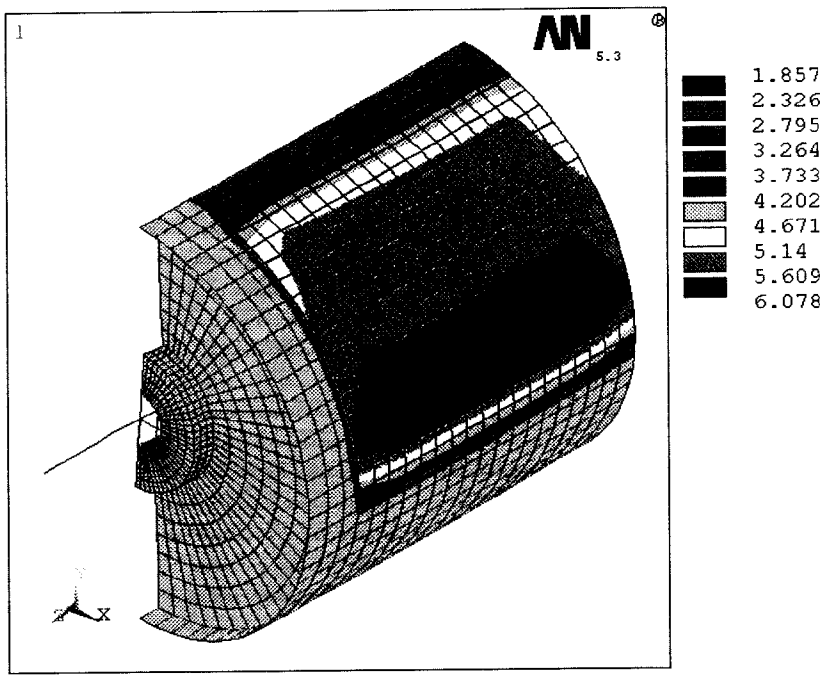

FIGURE 5.8 Tangential force distribution on roll body

The tangential forces also vary somewhat in the radial direction from 1.857 lb to 6.078 lb and only slightly in the longitudinal direction, similar to the normal force distribution. Together Figures 5.6 and 5.8 make up the total force distribution on the roll as a result of the tension in the strip.

The stresses in the accumulator roll can be adequately presented by showing the typical stress trends in each base model and then tabulating the stress values for each variation of the base models. The most significant stresses occur in the roll body and end plate of the roll. The next three Figures show the von Mises stress in the roll body only, for the three different base models analyzed.

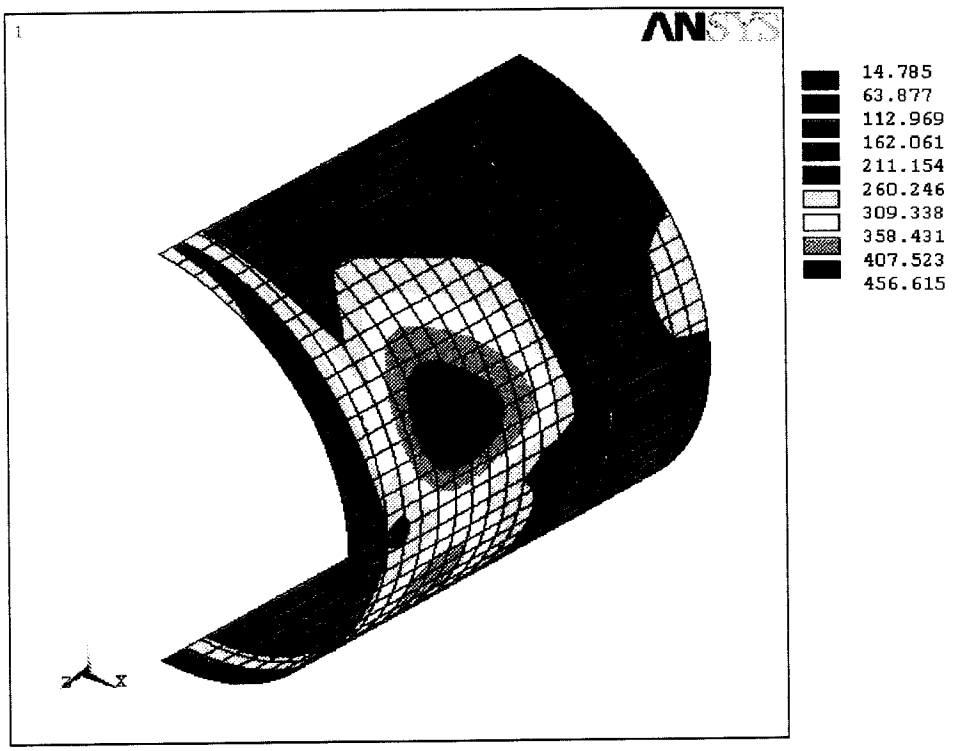

FIGURE 5.9 Case 1a von Mises stress in roll body

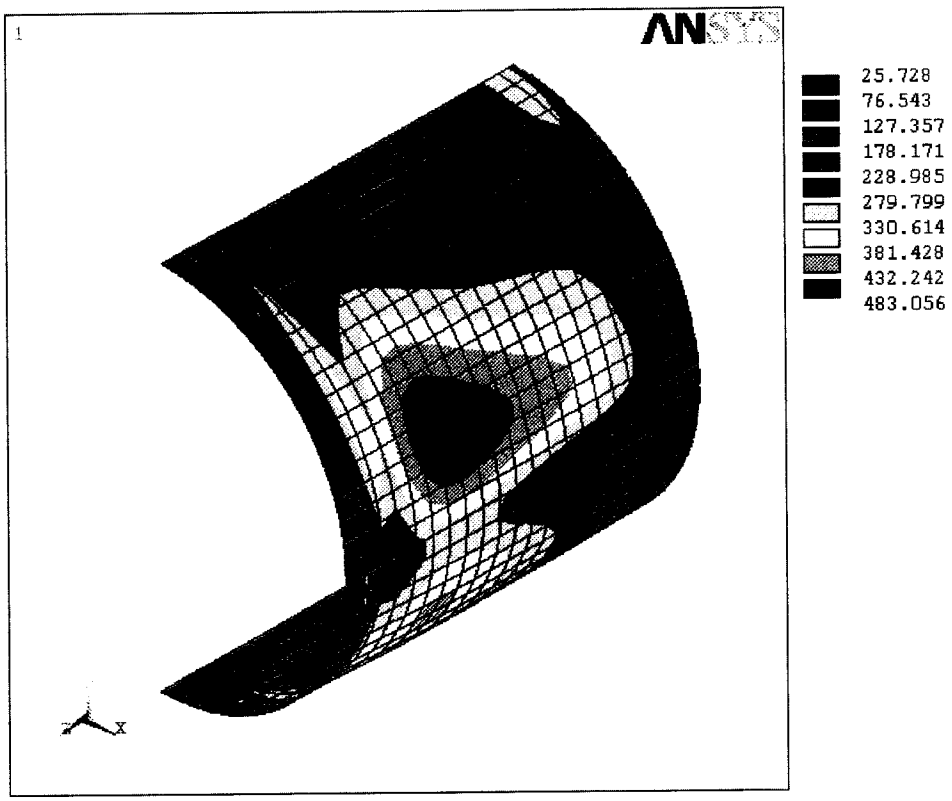

FIGURE 5.10 Case 2a von Mises stress in roll body

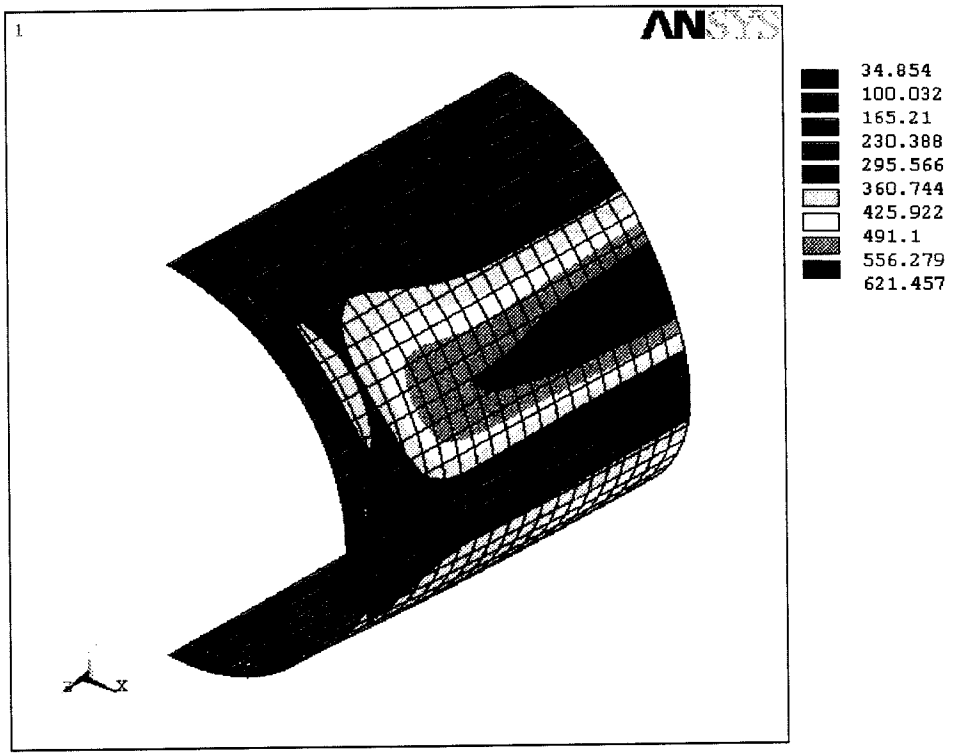

FIGURE 5.11 Case 3a von Mises stress in roll body

The maximum von Mises stress in the roll body for Case 1a is 456.6 psi and occurs at a longitudinal location closer to the end plate than the center of the roll. The maximum von Mises stress in the roll body for Case 2a is 483.1 psi and it also occurs at a longitudinal location closer to the end plate than the center of the roll. For Case 3a the maximum von Mises stress in the roll body is 621.5 psi but it occurs longitudinally at the center of the roll body. From the three base models with the original roll configuration, the stiffener doesn't seem to make a significant difference in maximum stresses and the location at which they occur for one or two stiffener rolls. However there is a difference when the stiffener is removed as in Case 3a; which produces higher stresses and moves the location of the maximum stress to the center of the roll. The von Mises stress in the end plates are shown in the next three Figures for the three base models.

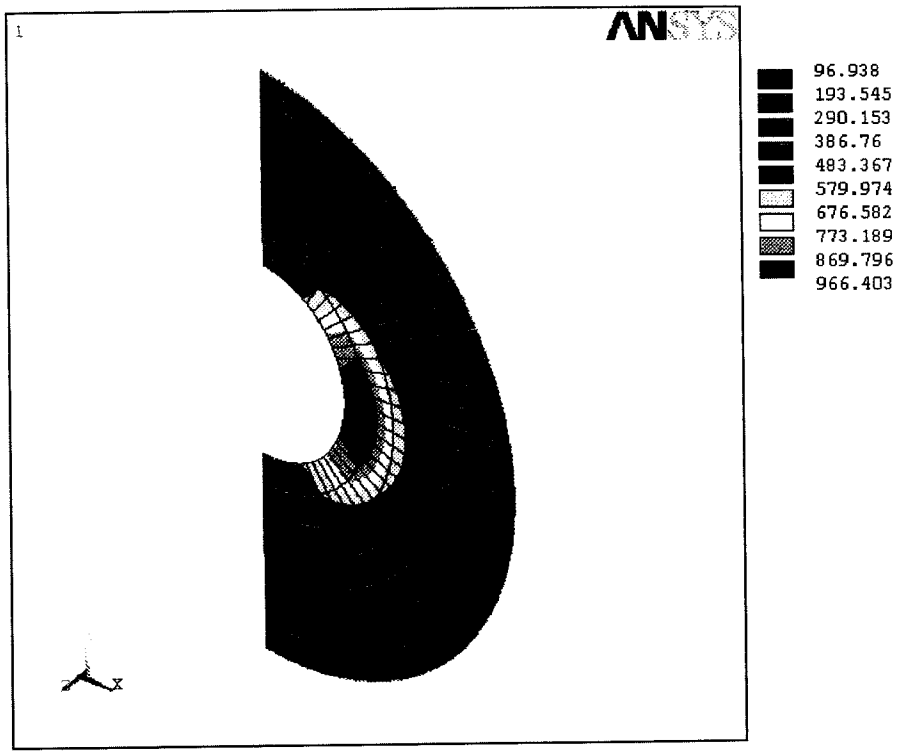

FIGURE 5.12 Case 1a von Mises stress in end plate

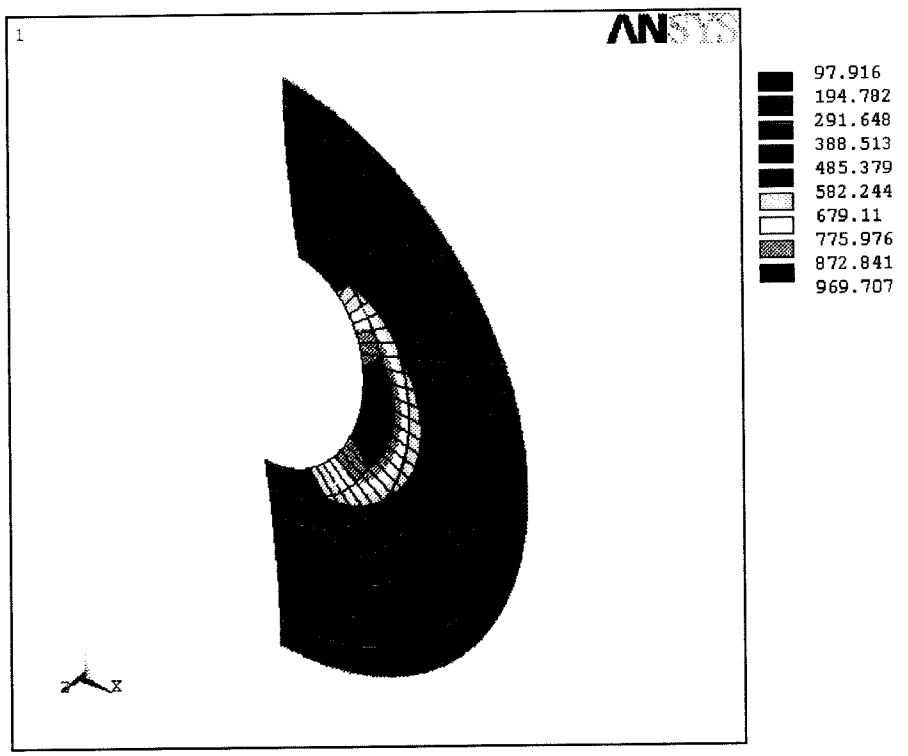

FIGURE 5.13 Case 2a von Mises stress in end plate

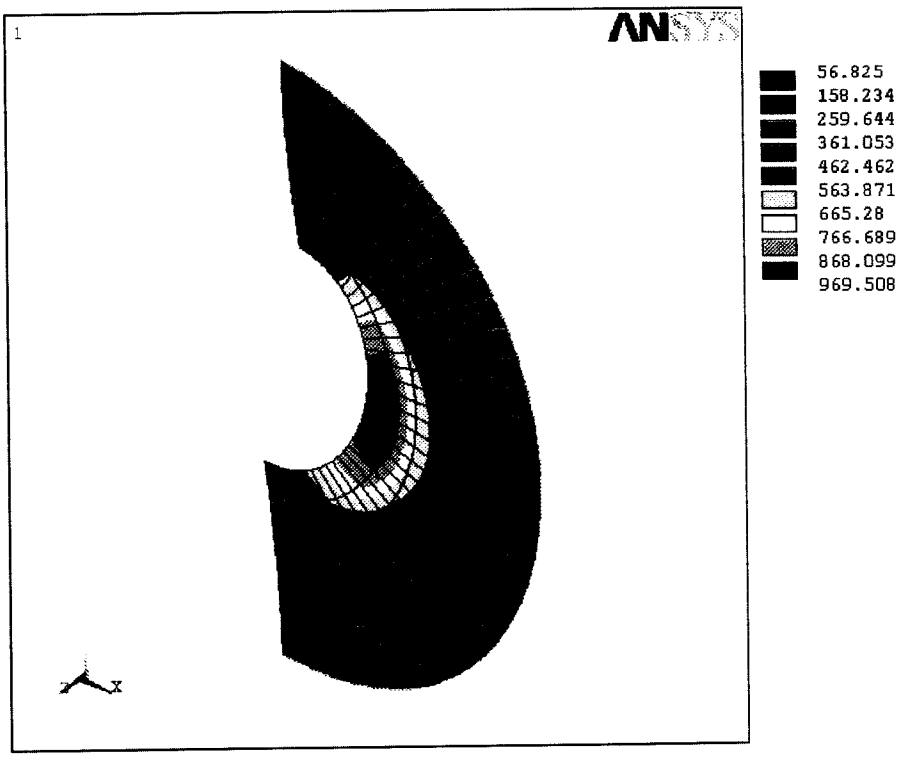

FIGURE 5.14 Case 3a von Mises stress in end plate

As can be seen in Figures 5.12 to 5.14 the maximum von Mises stress in the end plate varies only slightly for the three different stiffener configurations. The following table lists the maximum stress in each component of the roll for each base model and all the variations of the base models.

TABLE 5.2 Maximum stress in the roll components

Case	Max von Mises Stress (psi)				Max Stress (psi)
	End Plate	Roll Body	Stiffener	Hub	Shaft
1a	966	457	307	698	193
1b	1050	461	306	699	217
1c	960	639	407	698	198
2a	970	482	341	690	193
2b	1060	486	341	701	217
2c	961	677	460	699	198
3a	970	622	NA	694	193
3b	1060	625	NA	704	217
3c	947	951	NA	703	198

An interesting note about the end plate stresses is that considering how the roll is loaded, it would be expected that maximum compressive stresses in the endplate would occur at the top of the hub and maximum tensile stresses would occur at the bottom of the hub. That is not the case here because the highest von Mises stress occurs at the midpoint of the hub due the high component of shear stress located there. These shear stresses develop because there is a lot of distortion of the end plate, but it is rigidly held by the hub and roll body so consequently a complex stress state develops which gives rise to these shear stresses.

The most significant deflections are of the roll body and end plate. These can best be presented by showing the profile of each base model and then tabulating the deflections of the other variations of the base models. The next three figures show the deflected profile of the three base models.

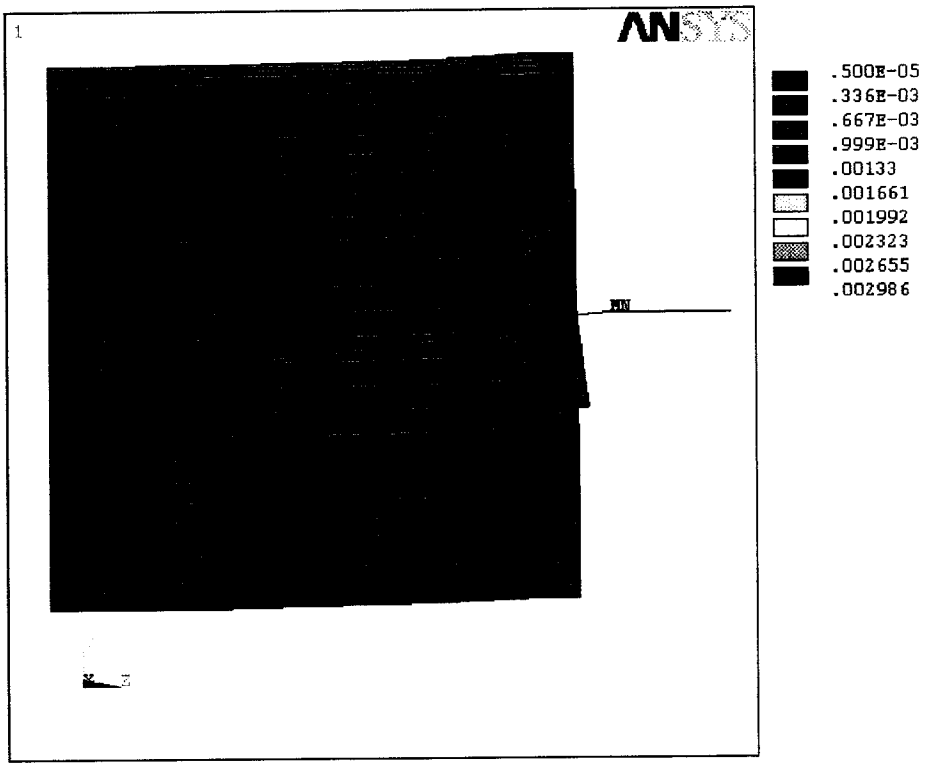

FIGURE 5.15 Case 1a deflection profile

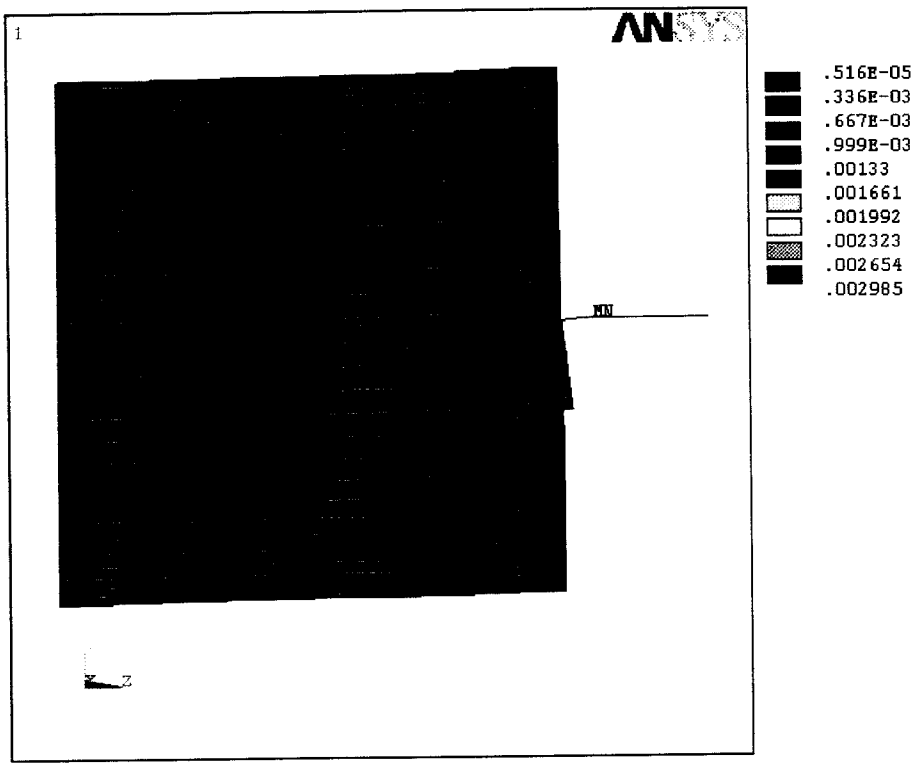

FIGURE 5.16 Case 2a deflection profile

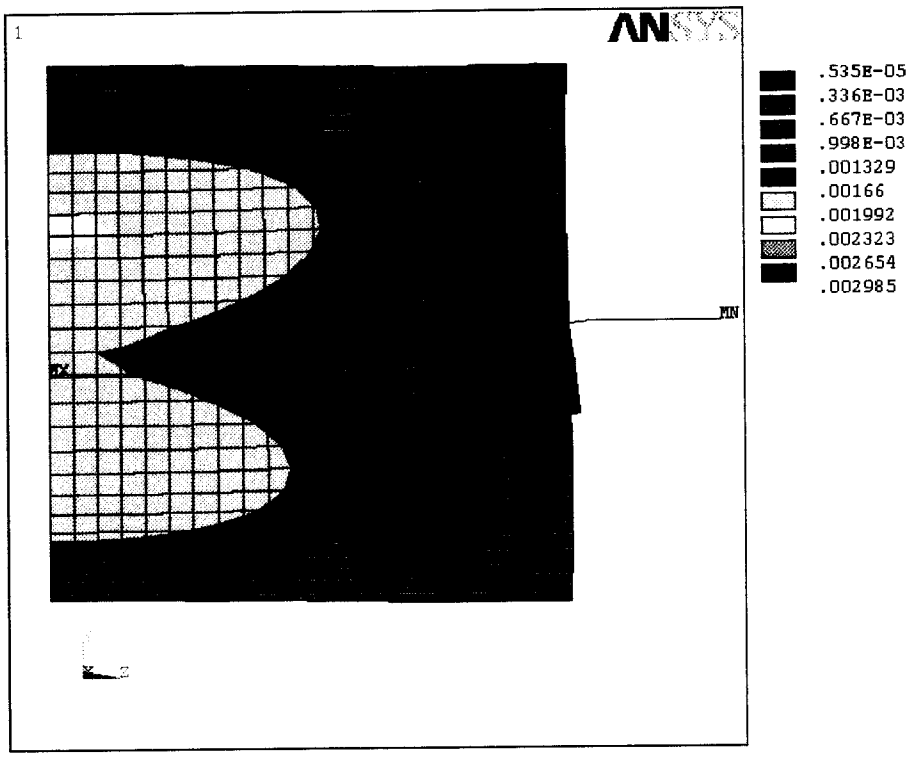

FIGURE 5.17 Case 3a deflection profile

From close inspection of Figures 5.15 to 5.17 it can be seen that the deflection profiles of the end plates are almost identical. The deflection profiles of the roll bodies are similar for the two rolls with the stiffeners and almost opposite to that of the roll without stiffeners. The stiffeners help keep the roll body circular and in Figure 5.17 with the absence of the stiffener, there is more deflection lower in the roll body; which actually causes the top of the roll body to rise above the end of the roll body. The deflections, like the stresses, are low with the maximum deflection of approximately 0.003" occurring at the midpoint of the shaft. Considering relative deflections of the roll body are critical to strip wrinklage the deflections of the roll body for the three base models where looked at and are shown in Figures 5.18 to 5.19.

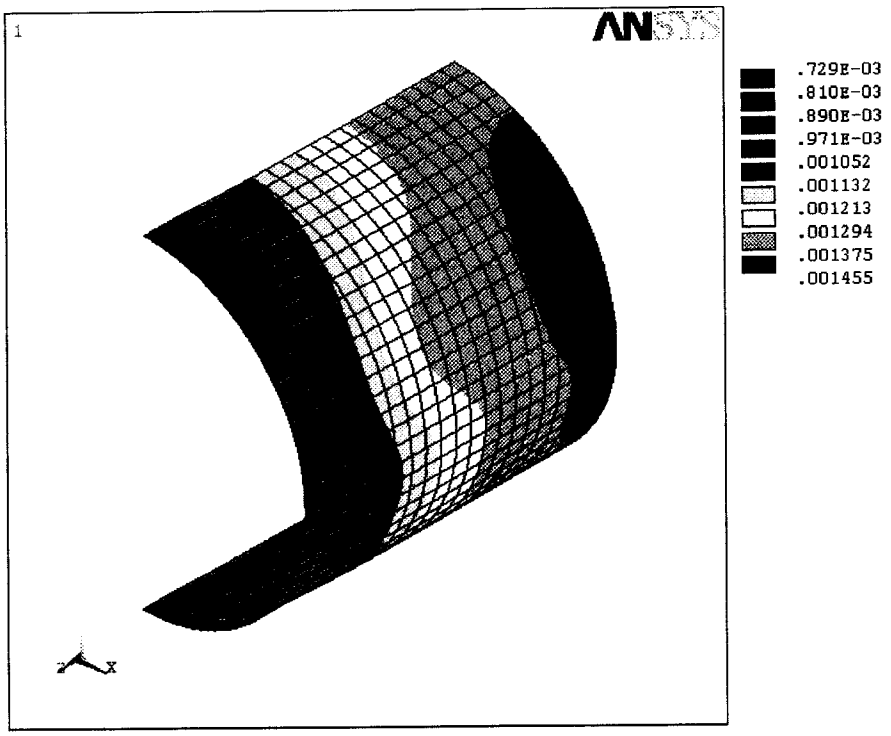

FIGURE 5.18 Case 1a roll body deflections

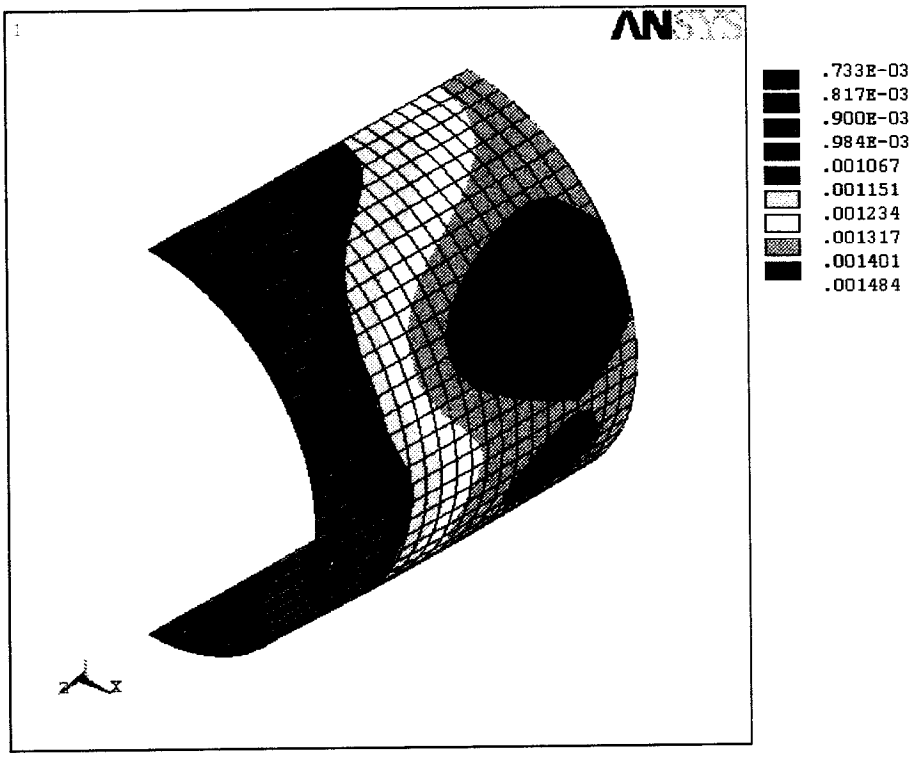

FIGURE 5.19 Case 2a roll body deflections

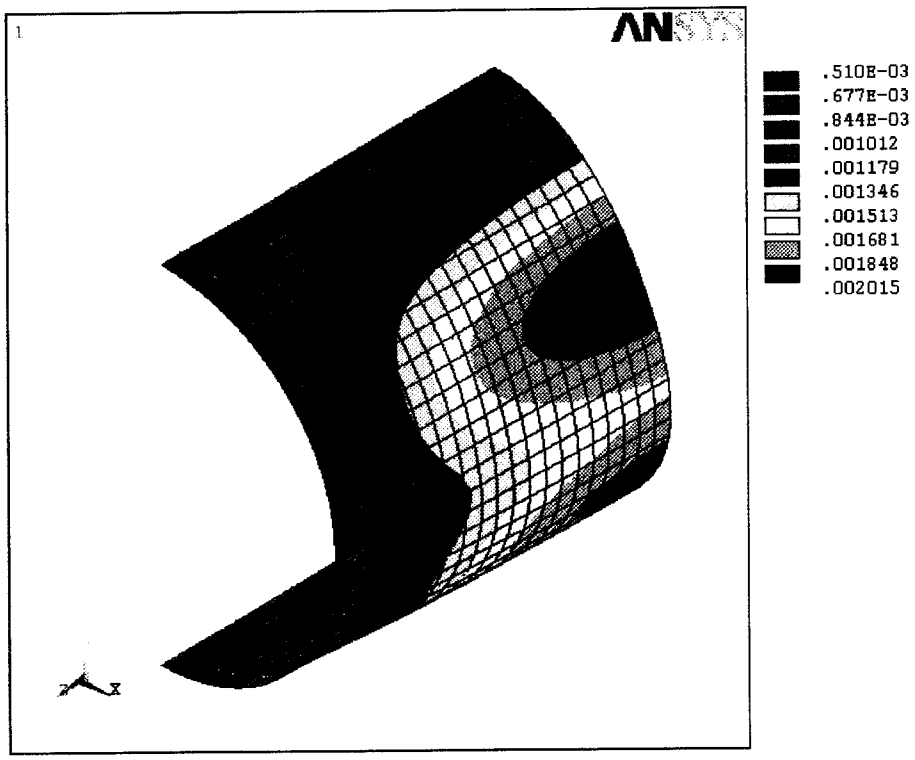

FIGURE 5.20 Case 3a roll body deflections

Chapter 6: COMPARISON & DISCUSSION

6.1 STRESSES

The stress results of the two analyses, meaning the linear analysis with uniform loading and the nonlinear analysis with frictional contact loading, are shown in Table 6.1. After reviewing the stress results of both analyses it was apparent that both predict low stresses in all components of the roll.

TABLE 6.1 Maximum stresses in the critical components of the roll

Case	Max von Mises Stress (psi)			
	Frictional Contact Loading		Uniform Pressure Loading	
	End Plate	Hub	End Plate	Hub
1a	966	698	1460	796
1b	1050	699	1740	819
1c	960	698	1450	780
2a	970	690	1460	795
2b	1060	701	1730	818
2c	961	699	1450	782
3a	970	694	1460	796
3b	1060	704	1730	818
3c	947	703	1490	799

As far as the stresses are concerned it is obvious that they seem too low to predict any damaging effects. It must be remembered that these results establish a trend that targets the endplate and hub as the critical regions of the roll. The actual hub to endplate interface is the most suitable location for fatigue failures to occur; when elevated stresses are present due to increased loading and thinner roll components. There is a difference in the corresponding values of the two analyses but both are too low to make any general statements about

why, considering the complex stress states that arise in this model and the different modeling techniques. It is important to remember the assumptions these stresses are based on and that this does not guarantee failures will not occur, because many other factors influence failures, such as impact loading from inconsistencies in line speeds, surface conditions, and material.

6.2 DEFLECTIONS

To compare the results of this analysis to the results of the previous analysis the deflections were plotted on the same graphs. As expected the deflections are low but are worth discussing considering relative deflections of the roll body could cause strip wrinklage, and to gain insight on deflection trends that occur in the different roll configurations. The figures, shown in the following pages, are plots of the deflection of the top line of nodes of the roll body for the all the cases considered. Even though the top line of nodes were not the location of maximum deflection in all models they were chosen as a location of comparison of the two different analyses. Note in the figures the two different analyses are referred to as ANSYS® and Algor®. The first plot, Figure 6.1, shows the deflections of the three base models Cases 1a, 2a, and 3a. The next three plots, Figures 6.2 to 6.4, show the deflections for the models with the endplate thickness varied; Cases 1b, 2b, and 3b. Finally the last three plots, Figures 6.5 to 6.7 show the deflections for the models with the roll body thickness varied; Cases 1c, 2c, and 3c.

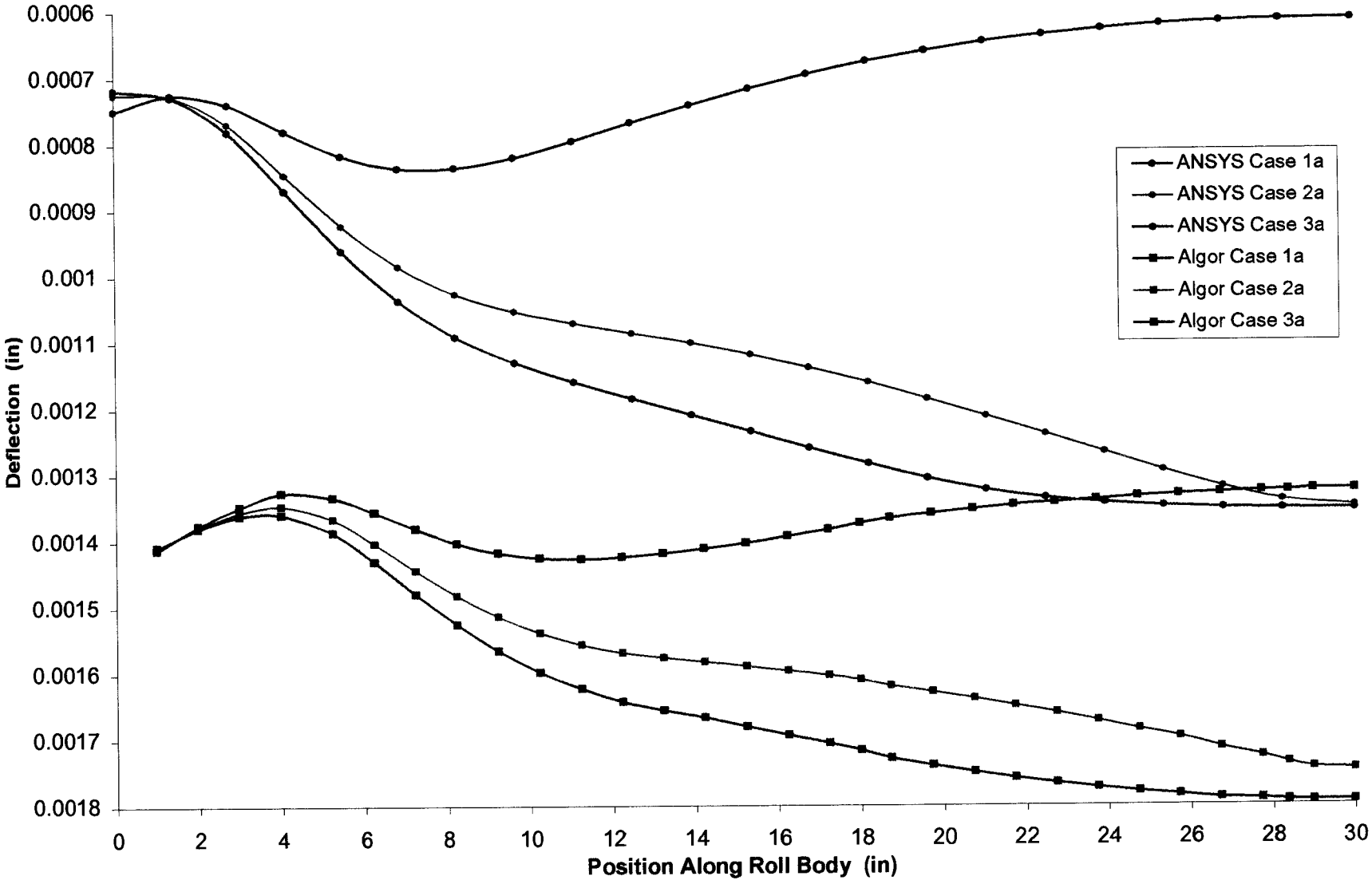

FIGURE 6.1 Deflection profile for Cases 1a, 2a, and 3a for both ANSYS® and Algor®

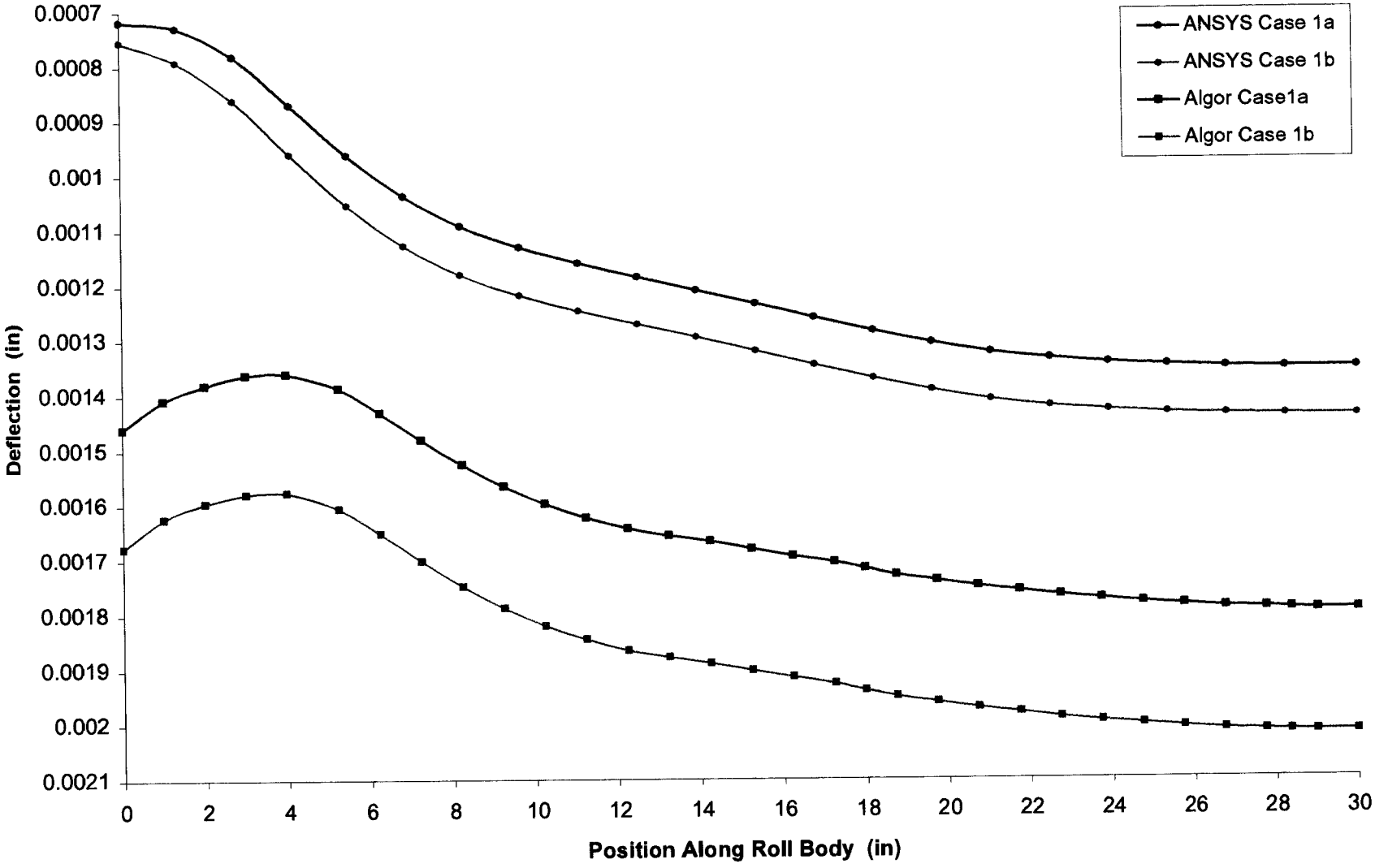

FIGURE 6.2 Deflection profile for Cases 1a and 1b for both ANSYS® and Algor®

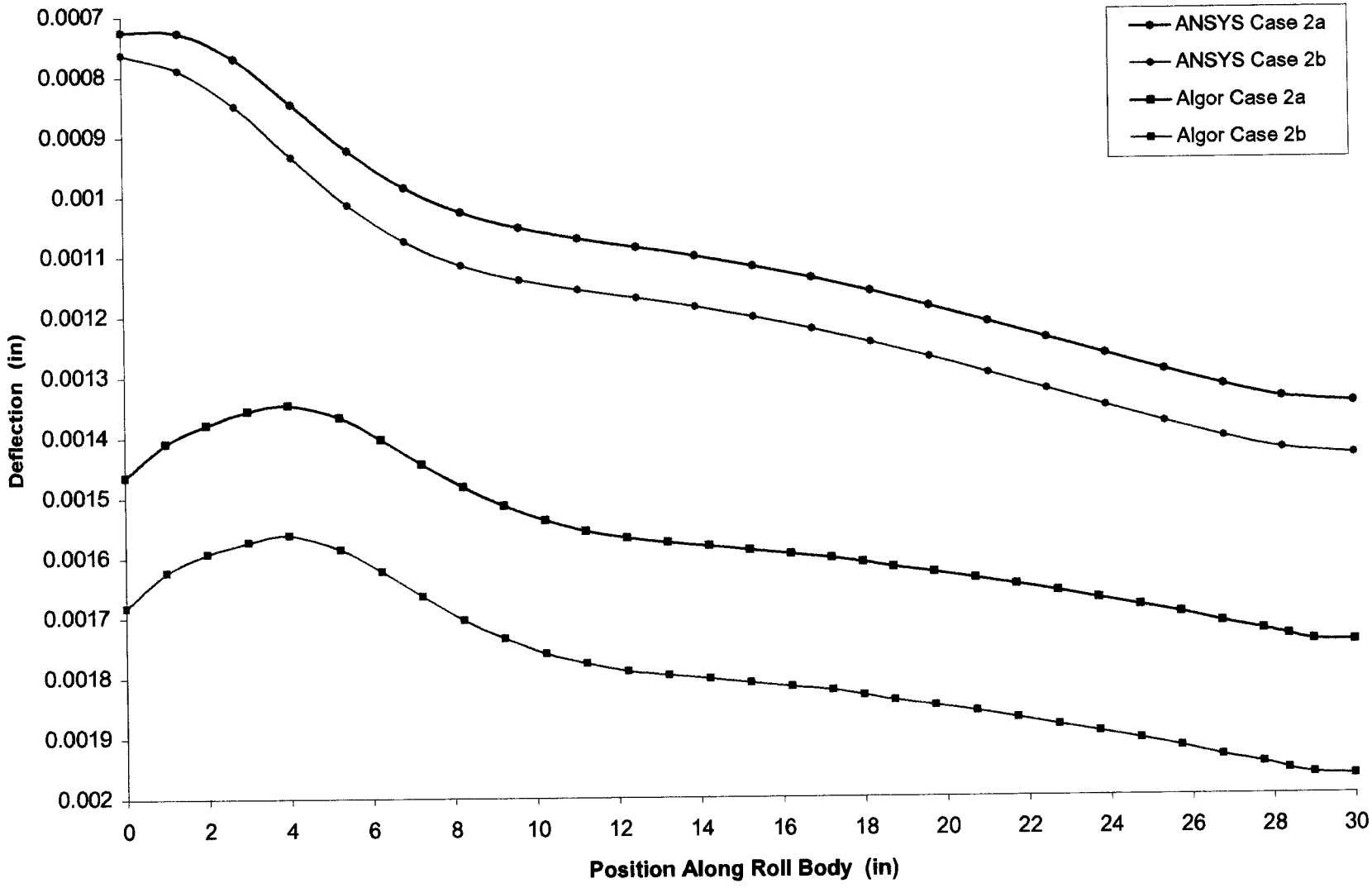

FIGURE 6.3 Deflection profile for Cases 2a and 2b for both ANSYS® and Algor®

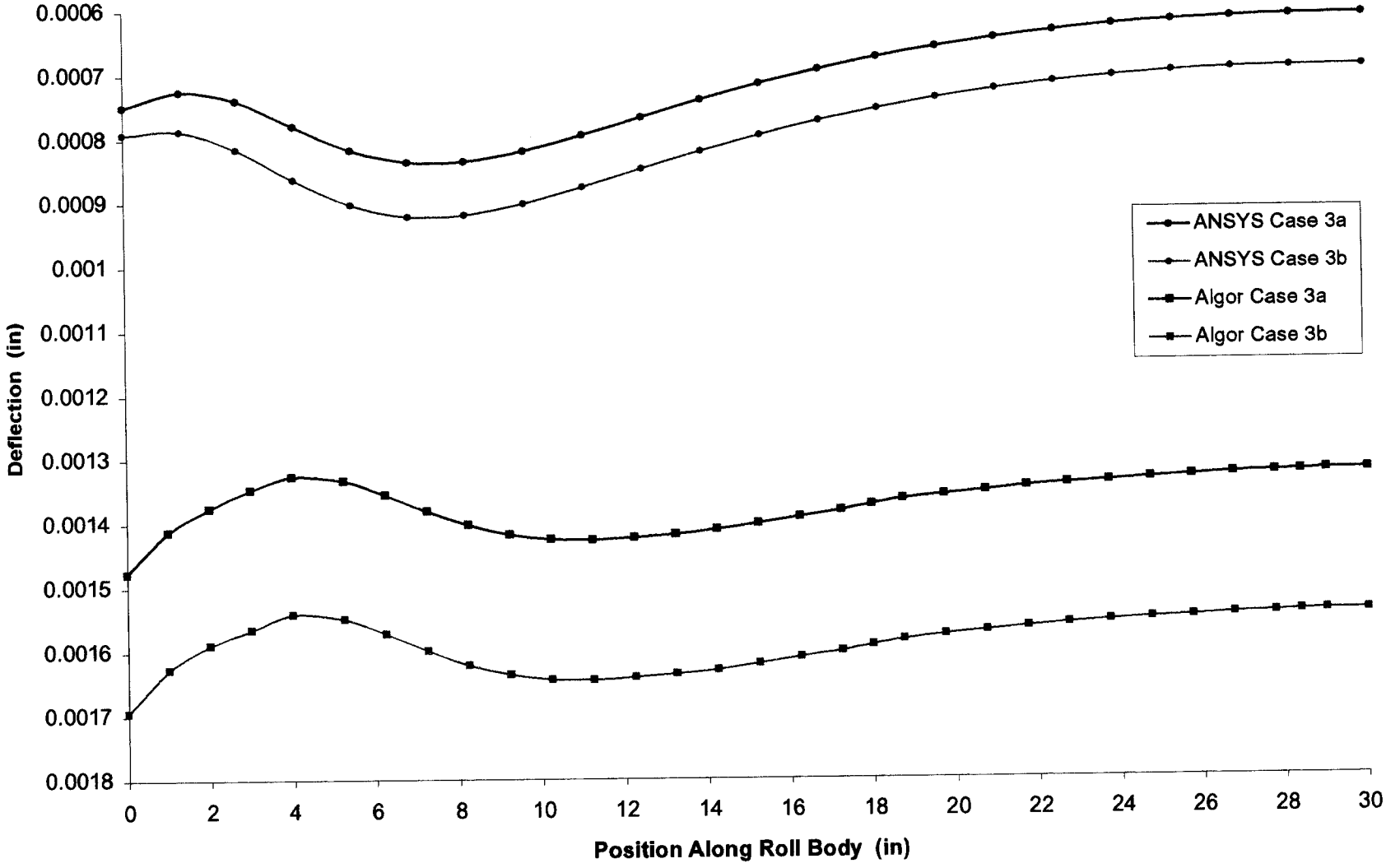

FIGURE 6.4 Deflection profile for Cases 3a and 3b for both ANSYS® and Algor®

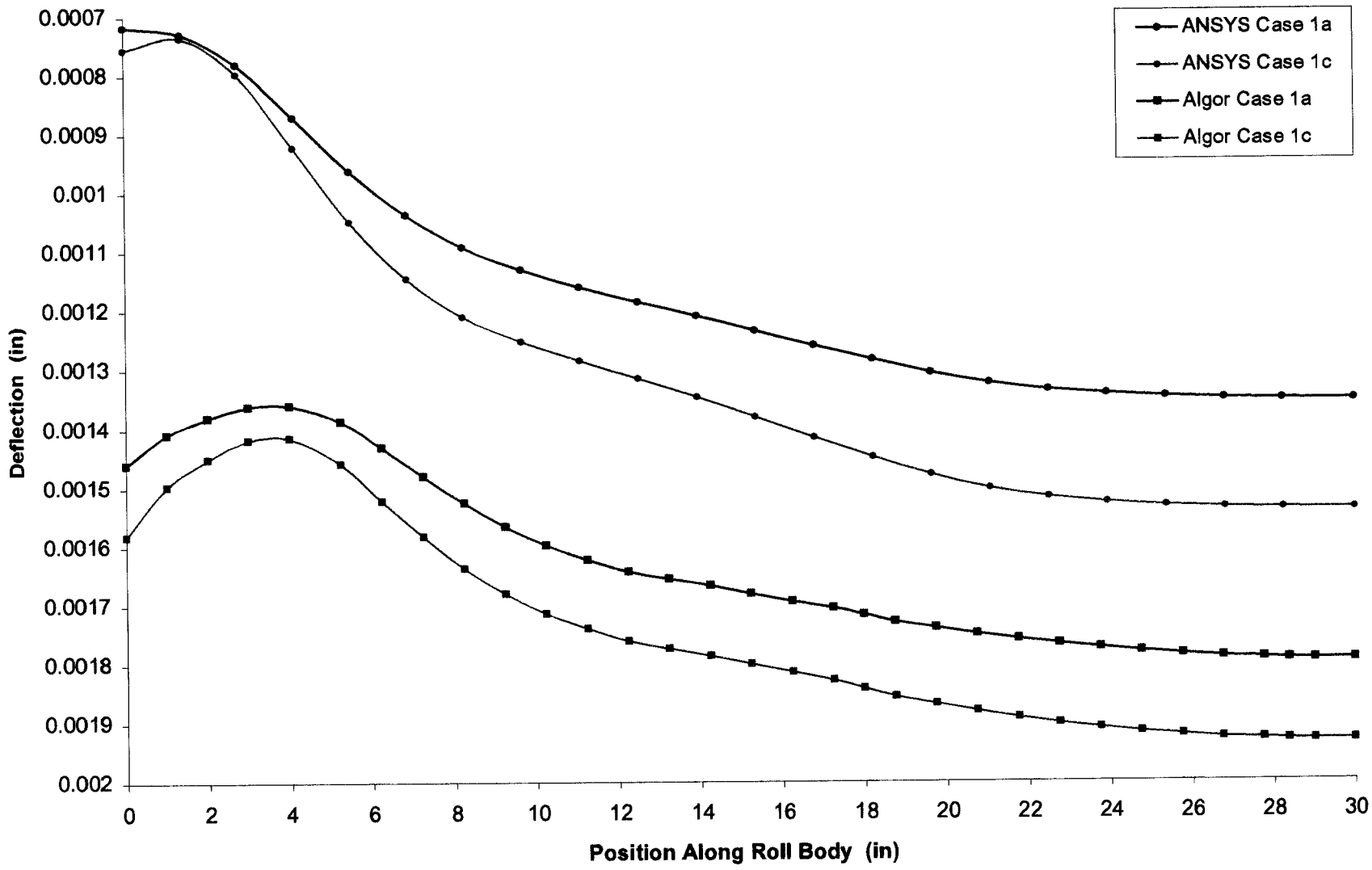

FIGURE 6.5 Deflection profile for Cases 1a and 1c for both ANSYS® and Algor®

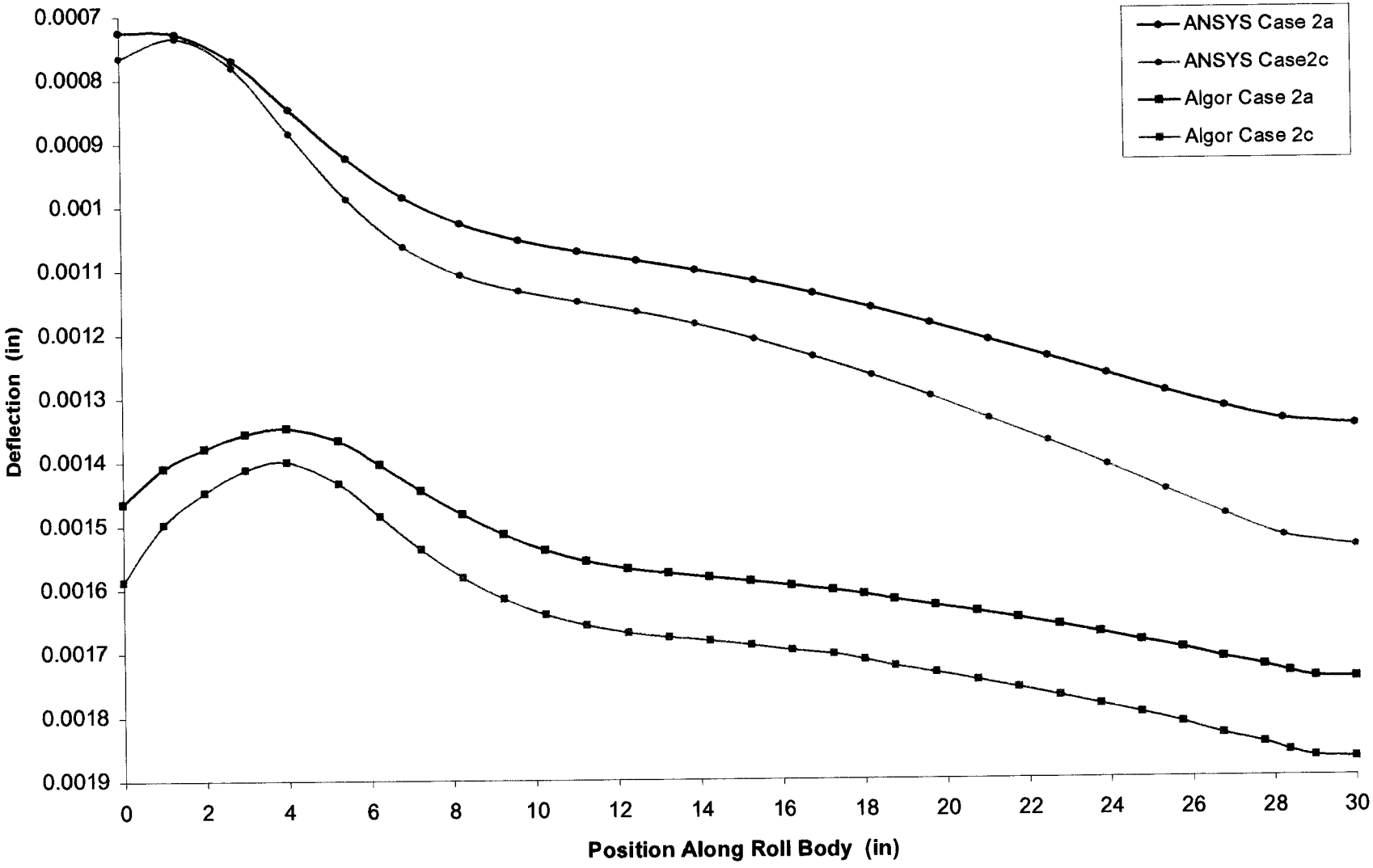

FIGURE 6.6 Deflection profile for Cases 2a and 2c for both ANSYS® and Algor®

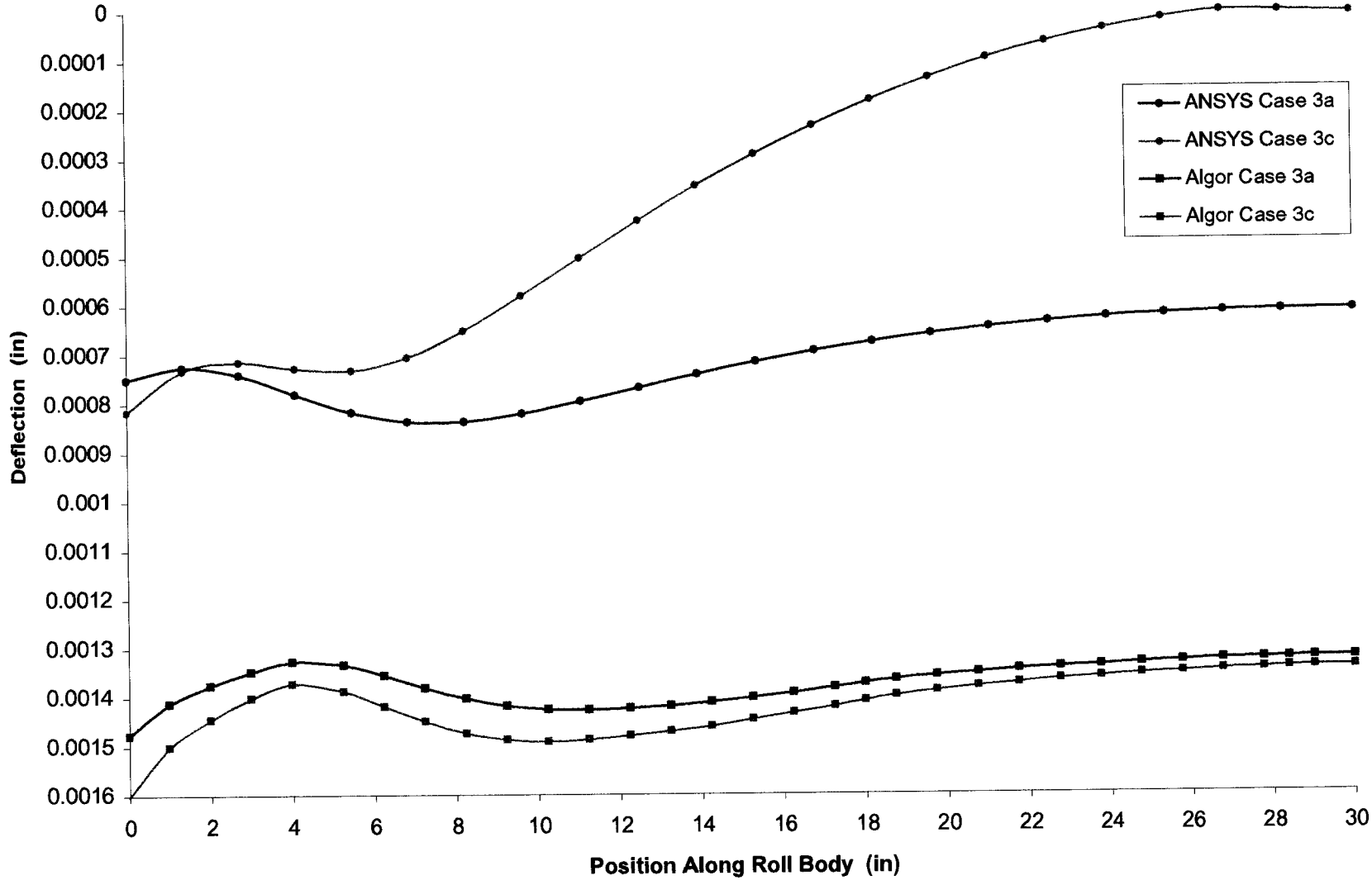

FIGURE 6.7 Deflection profile for Cases 3a and 3c for both ANSYS® and Algor®

The deflection profiles of Figure 6.1 show a similar trend in the deflections of the three base models Case 1a, Case 2a, and Case 3a for the respective analyses. There is a maximum absolute difference between them of about 0.0007", which could be attributed to different modeling techniques and the different analyses. Relative deflections are very similar for the two analyses. Case for case the profiles are almost exactly the same except for Case 3a where the relative deflection is more for the frictional contact loading model than the uniform pressure loading model, but only about 0.00012". This is due mainly to the fact that the frictional model has more of its load lower on the roll body due to the uneven load distribution. The deflection profiles of Figures 6.2 to 6.7 also show very similar profiles with the only major difference being the absolute differences. Based on these results it can be suggested, depending on deflection design criteria, that elimination of the stiffeners is possible or the use of only one stiffener at the center of the roll body would be adequate. Also thinning of the members like the roll body and endplate would also be possible but again would depend on design criteria and many other factors.

6.3 LOAD DISTRIBUTION

The load distribution developed in this study to predict the loading on the roll was shown in Figures 5.6 through 5.8. This distribution is made up of normal and tangential forces. It is clear to see the majority of the load is normal and not much different from that of a uniform radial distribution. Although the tangential stresses are dependent on the friction between the strip and roll, and therefore

dependent on the coefficient of friction used in the model, frictional effects seem to be of little significance to the design of critical areas of the roll.

6.4 CONCLUSIONS

There are three significant conclusions that can be drawn from the research that was done.

- Both analyses, the frictional contact loading and the uniform pressure loading, arrive at low numeric values for both stresses and deflections, but percent differences between the values are significant. Although for the roll configurations considered the values seem to low to make a difference, as loads increase and roll components are thinned these differences will be magnified when stresses and deflections reach critical values. This means that before any general conclusions about accumulator roll design can be made more investigation of a wider spectrum of roll configurations should be analyzed using frictional contact loading.
- The results from the uniform pressure loading analysis should be interpreted from a comparison perspective; meaning that those results can be used to gain insight on how the stresses and deflections behave as roll components and roll configurations are varied. If these variations cause stresses

and deflections to approach critical values then the more accurate frictional contact loading model should be used.

- The hub-to-end plate connection is targeted as the most likely location for fatigue failures to occur when stress levels increase to critical levels.

Another factor to consider is performing experimental work on actual working accumulator rolls using strain gages located in the region of the hub and end plate connection. This would be useful if more insight is desired on the actual stress states that develop in this area. Also if it is desired to thin down the end plate then reinforcement of the end plate-to-hub connection should be made. One way of accomplishing this is by attaching gusset plates between the hub and end plates on both sides of the end plate at different angle increments.

REFERENCES

[1] Giannakopoulos, A. E. "The Return Mapping Method for the Integration of Friction Constitutive Relations", *Computers and Structures*, Vol. 32, pp. 157-167 (1989)

[2] Hibbeler, R. C. Engineering Mechanics - Statics. New York: Macmillan Publishing Company, 1992.

[3] Kinnavy, M. G. "Design Considerations in Tension Leveling Systems", *Iron and Steel Engineer*, Oct. 1990.

[4] ANSYS Analysis Guides. ANSYS Help System Release 5.4. SAS IP, Inc., 1997.

[5] ANSYS Elements Reference. ANSYS Help System Release 5.4. SAS IP, Inc., 1997.

[6] ANSYS Theory Reference. ANSYS Help System Release 5.4. SAS IP, Inc., 1997.

APPENDIX

TABLE A.1 Variation of stiffener location

MODEL NAME	ROLL CONFIGURATION				
	NUMBER OF STIFFENERS	STIFFENER LOCATION (z1)	STIFFENER THICKNESS (t1)	ROLL BODY THICKNESS (t2)	END PLATE THICKNESS (t3)
ads6z	0	none	none	1	1.25
ads5z	1	0	0.5	1	1.25
ads7z5	2	6.25	0.5	1	1.25
ads3z	2	8.25	0.5	1	1.25
ads7z1	2	10.25	0.5	1	1.25
ads7z2	2	12.25	0.5	1	1.25
ads7z3	2	14.25	0.5	1	1.25
ads7z4	2	16.25	0.5	1	1.25

TABLE A.2 Variation of stiffener thickness

MODEL NAME	ROLL CONFIGURATION				
	NUMBER OF STIFFENERS	STIFFENER LOCATION (z1)	STIFFENER THICKNESS (t1)	ROLL BODY THICKNESS (t2)	END PLATE THICKNESS (t3)
ads3z	2	8.25	0.5	1	1.25
ads8z	2	8.25	0.75	1	1.25
ads10z	2	8.25	1	1	1.25
ads5z	1	0	0.5	1	1.25
ads9z	1	0	0.75	1	1.25
ads11z	1	0	1	1	1.25

TABLE A.3 Variation of roll body thickness

MODEL NAME	ROLL CONFIGURATION				
	NUMBER OF STIFFENERS	STIFFENER LOCATION (z1)	STIFFENER THICKNESS (t1)	ROLL BODY THICKNESS (t2)	END PLATE THICKNESS (t3)
ads27z	2	8.25	0.5	0.5	1.25
ads24z	2	8.25	0.5	0.75	1.25
ads3z	2	8.25	0.5	1	1.25
ads12z	2	8.25	0.5	1.125	1.25
ads15z	2	8.25	0.5	1.25	1.25
ads30z	2	8.25	0.5	1.5	1.25
ads33z	2	8.25	0.5	1.75	1.25
ads36z	2	8.25	0.5	2	1.25
ads28z	1	0	0.5	0.5	1.25
ads25z	1	0	0.5	0.75	1.25
ads5z	1	0	0.5	1	1.25
ads13z	1	0	0.5	1.125	1.25
ads16z	1	0	0.5	1.25	1.25
ads31z	1	0	0.5	1.5	1.25
ads34z	1	0	0.5	1.75	1.25
ads37z	1	0	0.5	2	1.25
ads29z	0	none	none	0.5	1.25
ads26z	0	none	none	0.75	1.25
ads6z	0	none	none	1	1.25
ads14z	0	none	none	1.125	1.25
ads17z	0	none	none	1.25	1.25
ads32z	0	none	none	1.5	1.25
ads35z	0	none	none	1.75	1.25
ads38z	0	none	none	2	1.25

TABLE A.4 Variation of end plate thickness

MODEL NAME	ROLL CONFIGURATION				
	NUMBER OF STIFFENERS	STIFFENER LOCATION (z1)	STIFFENER THICKNESS (t1)	ROLL BODY THICKNESS (t2)	END PLATE THICKNESS (t3)
ads41z	2	8.25	0.5	1	1
ads40z	2	8.25	0.5	1	1.125
ads3z	2	8.25	0.5	1	1.25
ads18z	2	8.25	0.5	1	1.375
ads21z	2	8.25	0.5	1	1.5
ads39z	2	8.25	0.5	1	1.625
ads44z	1	0	0.5	1	1
ads43z	1	0	0.5	1	1.125
ads5z	1	0	0.5	1	1.25
ads19z	1	0	0.5	1	1.375
ads22z	1	0	0.5	1	1.5
ads42z	1	0	0.5	1	1.625
ads47z	0	none	none	1	1
ads46z	0	none	none	1	1.125
ads6z	0	none	none	1	1.25
ads20z	0	none	none	1	1.375
ads23z	0	none	none	1	1.5
ads45z	0	none	none	1	1.625

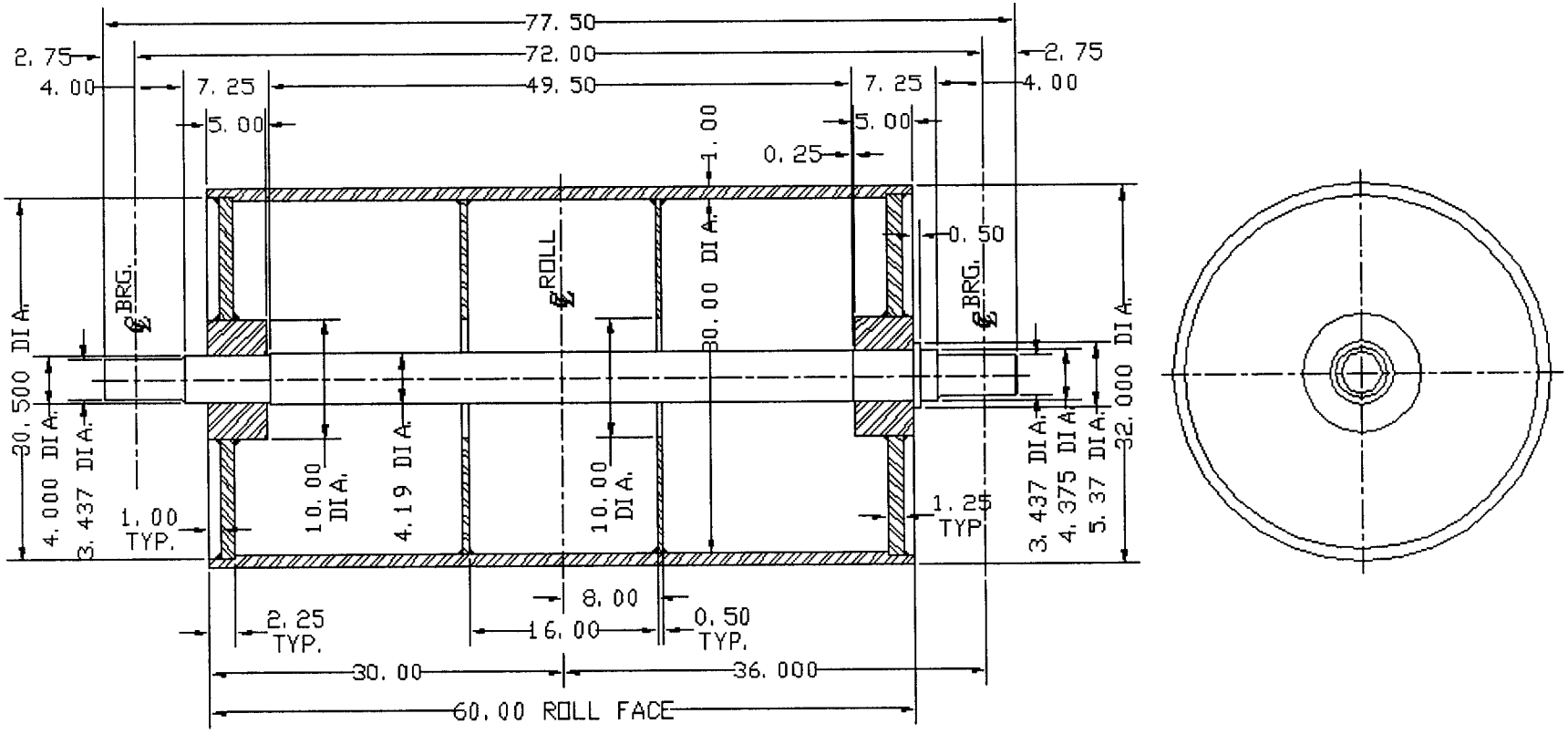

FIGURE A.1 Drawing of roll analyzed in this research